TECHNISCHE UNIVERSITÄT WIEN
Vienna University of Technology

**DIPLOMARBEIT**

# Creation of a stable gel wax phantom for the clinical multi-spectral optoacoustic imaging device MSOT Acuity Echo

zur Erlangung des akademischen Grades

**Diplom-Ingenieurin**

im Rahmen des Studiums

**Biomedical Engineering**

eingereicht von

**Nastasia Turek, BSc**

Matrikelnummer 01125564

ausgeführt am Institut für Angewandte Physik
der Fakultät für Physik der Technischen Universität Wien
in Zusammenarbeit mit iThera Medical GmbH

**Betreuung**
Betreuer: Dipl. Ing. Stefan **MORSCHER**
Begutachter: Ao.Univ.Prof. Dipl.-Ing. Dr.techn. Martin **GRÖSCHL**

Mödling, 16.12.2024 _____ _____
(Nastasia Turek) (Martin Gröschl)

## Abstract

This study explores the development of a calibration phantom tailored to the requirements of optoacoustic imaging, specifically for the MSOT Acuity Echo system. A manufacturing process for a gel wax-based phantom was established and the reproducibility and stability of a Zerdine phantom were assessed to evaluate its potential as a calibration tool. The investigation primarily concentrated on the design and evaluation of the phantoms, excluding broader considerations of system-wide calibration or clinical implementation.

Key findings include quantifiable variations in laser pulse energy, signal reproducibility and imaging metrics. Laser energy stability exhibited in-study and overall variations of 1.23% and 11.03%, respectively, while absorber signal variability ranged from 1.58% to 11.87%. The analysis revealed significant dependencies of image signals on target absorption properties, with higher absorption resulting in uniformly elevated image intensities. Positional and directional variability of the ROI positioning showed that x-direction variability exceeded that of the y-direction, with in-study variations of 3.25% and 0.57%, respectively.

The gel wax phantom was developed with integrated absorbers, customizable optical properties and a 3D-printed protective casing, facilitating standardized manufacturing and user-friendly handling. However, potential uncertainties related to the consistency of commercially available gel wax and the long-term stability of its properties highlight areas for future investigation.

The findings suggest that the developed phantom has the potential to enhance device reliability and improve the precision of optoacoustic imaging. Future research could investigate alternative materials, explore a broader range of configurations and assess the phantom's performance in longitudinal studies to further refine its applications and evaluate its impact on clinical work-flows. This study provides a foundation for advancing calibration methods and optimizing optoacoustic imaging systems.

## Zusammenfassung

Diese Studie beleuchtet die Notwendigkeit eines Kalibrierungsphantoms, das speziell für die Anforderungen der optoakustischen Bildgebung entwickelt wurde, mit besonderem Augenmerk auf das MSOT Acuity Echo-System. Im Rahmen des Projekts wurde ein Herstellungsprozess für ein Gelwachs-basiertes Phantom etabliert und die Reproduzierbarkeit sowie Stabilität eines Zerdine-Phantoms untersucht, um dessen Potenzial als Kalibrierungsinstrument zu bewerten. Der Schwerpunkt lag dabei auf der Entwicklung und Evaluierung der Phantome, ohne jedoch eine vollständige Systemkalibrierung oder klinische Anwendung einzubeziehen.

Zu den zentralen Ergebnissen gehören quantifizierbare Schwankungen in der Laserpulsenergie, der Signalreproduzierbarkeit und verschiedenen Bildgebungsmetriken. Die Stabilität der Laserenergie wies während der Studie eine Schwankung von 1.23% und eine Gesamtschwankung von 11.03% auf. Die Variabilität der Absorbersignale lag zwischen 1.58% und 11.87%. Die Analyse zeigte eine klare Abhängigkeit der Bildsignale von den Absorptionseigenschaften des Absorbers, wobei eine höhere Absorption zu gleichmäßig gesteigerten Bildintensitäten führte. Die Positions- und Richtungsvariabilität der ROI-Positionierung zeigte, dass die Variabilität in x-Richtung (3.25%) größer war als in y-Richtung (0.57%).

Das Gelwachs-Phantom wurde mit integrierten Absorbern, anpassbaren optischen Eigenschaften und einem 3D-gedruckten Schutzgehäuse entwickelt, um eine standardisierte Fertigung und einfache Handhabung zu gewährleisten. Die Konsistenz des kommerziell erhältlichen Gelwachses und die Langzeitstabilität seiner Eigenschaften stellen mögliche Unsicherheitsfaktoren dar, die in zukünftigen Untersuchungen näher analysiert werden sollten.

Die Ergebnisse deuten darauf hin, dass das entwickelte Phantom dazu beitragen könnte, die Zuverlässigkeit von Geräten zu steigern und die Genauigkeit der optoakustischen Bildgebung zu verbessern. Zukünftige Studien könnten alternative Materialien, eine größere Vielfalt an Konfigurationen und die Leistungsbewertung des Phantoms in Längsschnittuntersuchungen in den Fokus nehmen. Ziel wäre es, weitere potenzielle Einsatzbereiche und den Einfluss auf klinische Abläufe zu untersuchen und zu optimieren. Diese Untersuchung bildet eine solide Basis für die Weiterentwicklung von Kalibrierungsmethoden und die Verbesserung optoakustischer Bildgebungssysteme.

# Contents

# 1 Introduction

Optoacoutic imaging combines the advantages of optical imaging with those of ultrasound imaging. It offers high spatial resolution of ultrasound and high contrast of optical imaging, which makes it possible to visualize tissue structures and functions non-invasively and in real-time. [1] It's potential clinical applications are vast, such as cancer detection, oxygen saturation measurement or vascular imaging. [2]

However, its clinical translation faces challenges such as limited depth penetration, light scattering and system variability, alongside the need for standardized calibration and validation protocols. [3] Accurate bio-marker quantification, essential for clinical applications, depends on precise calibration to address factors like wavelength-dependent absorption and tissue heterogeneity. [4]

Imaging devices across various modalities (e.g. computed tomography, magnetic resonance imaging, positron emission tomography) depend on calibration phantoms to verify the system's accuracy, ensuring consistent and reproducible results in clinical settings. These phantoms serve as reference standards to assess system performance, stability and imaging metrics under controlled conditions. [5]

Calibration phantoms are artificial models designed to mimic tissue properties, serving as essential tools for testing, standardizing and validating imaging systems. [6] In optoacoustic imaging, calibration is particularly complex due to its dual-modal nature, requiring precise alignment of optical absorption and acoustic signal generation across varying tissue types and wavelengths. [7, 8] As an emerging modality, optoacoustic imaging lacks standardized benchmarks, making phantoms indispensable for ensuring reproducibility and validating system performance. Existing phantom designs often fall short, focusing on either optical or acoustic properties and fail to address the dual-modal requirements or simulate complex tissue geometries. [9] The lack of a reliable calibration phantom in optoacoustic imaging leads to significant clinical and technological consequences, including inaccurate measurements, inconsistent results, reduced image quality and possible misinterpretation of bio-marker data, affecting clinical applicability and hindering the validation and comparison of new imaging systems with established methods.

The aim of this project was to address the absence of a suitable calibration phantom specifically designed for the requirements of optoacoustic imaging.

This work can be viewed as a step toward overcoming a critical bottleneck in the maturation of the MSOT Acuity Echo [10] by developing and testing an experimental procedure for manufacturing a calibration phantom.

The key aspects of this thesis are:

- Developing a manufacturing process for a gel wax phantom
- Conducting reproducibility and stability tests for a Zerdine phantom to evaluate its suitability as a calibration tool

The scope of this thesis is focused on the development and assessment of phantoms, rather than addressing comprehensive system calibration. While the work lays a foundation for improving calibration efforts, it does not extend to the full integration of these phantoms into broader system validation or clinical work-flows.

# 2 Theoretical Background

## 2.1 Optoacoustic Imaging

### 2.1.1 Past and Present of Optoacoustic Technology

Optoacoustics, also known as photoacoustics, describes the effect of acoustic wave generation by light absorption. The first use of this effect goes back into 1880, when Bell invented the first wireless telephone, an optical communication device, the photophone. [11] Later Tyndall and Roentgen confirmed the occurrence of the photoacoustic effect in gasses. [12, 13]

Only due to the development of laser technology and more sensitive microphones in the 1970s the optoacoustic imaging was pushed to a new level, the optoacoustic spectroscopy. [14] In 1981, Bowen presented spectroscopy of biological materials. [15] His approach to create a sound wave by radio-frequency electromagnetic radiation is today called thermoacoustics. [16]

In the 1990s Diebold et al. described the mathematical basis for the generated sound waves depending on the absorbing body and the duration of the laser pulse. [17–19] These relationships form the basis for the later development of reconstruction algorithms that ultimately made optoacoustic imaging possible.

Propelled by numerous unmet needs in biology and medicine, optoacoustic research has advanced rapidly in the mid-1990s, leading to the significant advancements in instrumentation systems, image reconstruction algorithms and capabilities for functional and molecular imaging providing non-invasive, label-free and non-ionizing solutions.

While optoacoustic imaging holds great promise as an imaging modality, it still faces several technological, clinical and regulatory challenges. [20] Technological challenges include the complexity of integrating optical and acoustic components, which must be precisely calibrated to ensure accurate imaging. Additionally, achieving optimal depth penetration while maintaining high spatial resolution, managing large volumes of data and improving real-time imaging capabilities remain significant hurdles for the technology's development and clinical implementation. Clinical challenges include slow translation to clinical use, regulatory hurdles, lack of standardized protocols, high costs and difficulties in integrating the technology into existing healthcare work-flows. [21]

### 2.1.2 Basic Concept of Optoacoustic Imaging

The underlying principle of optoacoustic imaging is the so called photoacoustic effect (Figure 1) It describes the generation of ultrasound waves in a material upon absorbing pulsed laser light, typically in the visible or near infra-red spectrum (400 $nm$ - 1200 $nm$). [2]

Modern optoacoustic imaging systems use lasers that generate ultra-short pulses in the range of 1 $nm$ - 100 $nm$, primarily because they enable improved signal-to-noise ratios. [22] As the pulsed light propagates through the tissue, the interaction of light is determined by absorption and scattering processes, resulting in localized heating. The temperature rise leads to thermo-elastic expansion which is followed by a pressure rise resulting in the emission of broadband (1 $MHz$ -

100 $MHz$) low-amplitude (less than 10 $kPa$) acoustic waves, known as photoacoustic waves. [23]

The generated pressure distribution $p_0(r)$ is proportional to the total absorbed optical energy density $H(r)$ [24]:

$$\boxed{p_0(r) = \Gamma \cdot H(r)} \tag{1}$$

with

$$H(r) = \mu_a(r) \cdot \Phi(r, \mu_a, \mu_s, g) \tag{2}$$

where $\Gamma$ is the dimensionless Grueneisen parameter, describing the efficiency of the conversion of light into heat and subsequently into a pressure wave and is given by $\Gamma = \beta c^2/C_p$ where $\beta$ is the coefficient of thermal volume expansion, $c$ is the speed of sound and $C_p$ is the specific heat capacity. The optical fluence $\Phi(r, \mu_a, \mu_s, g)$ represents the total energy delivered per unit area by a light source over a specific time period $[J/m^2]$. The absorption coefficient $\mu_a$, scattering coefficient $\mu_s$ and the anisotropic factor $g$ significantly influence the optical fluence in a medium by affecting how light propagates and attenuates within it.

These optoacoustic waves propagate through the tissue with minimal disturbance to the surface where they are detected by ultrasound transducers. [25] Piezoelectric ultrasound detectors are the most commonly employed in optoacoustic imaging due to their high sensitivity, low thermal noise and broad bandwidth capabilities, which can reach up to 100 $MHz$. [26]

The detected signals, known as A-line signals, represent the transducer's time-dependent response to the ultrasound wave. By processing and combining multiple A-line signals, a detailed 2D optoacoustic image of the tissue can be generate. [27] The image contrast depends on the distribution of absorbed optical energy, which in turn is influenced by the wavelengths of light used and the optical properties of the specific tissue. The result is an image that reflects variations in optical absorption within the tissue, enabling detailed mapping of its structure and composition. [28]

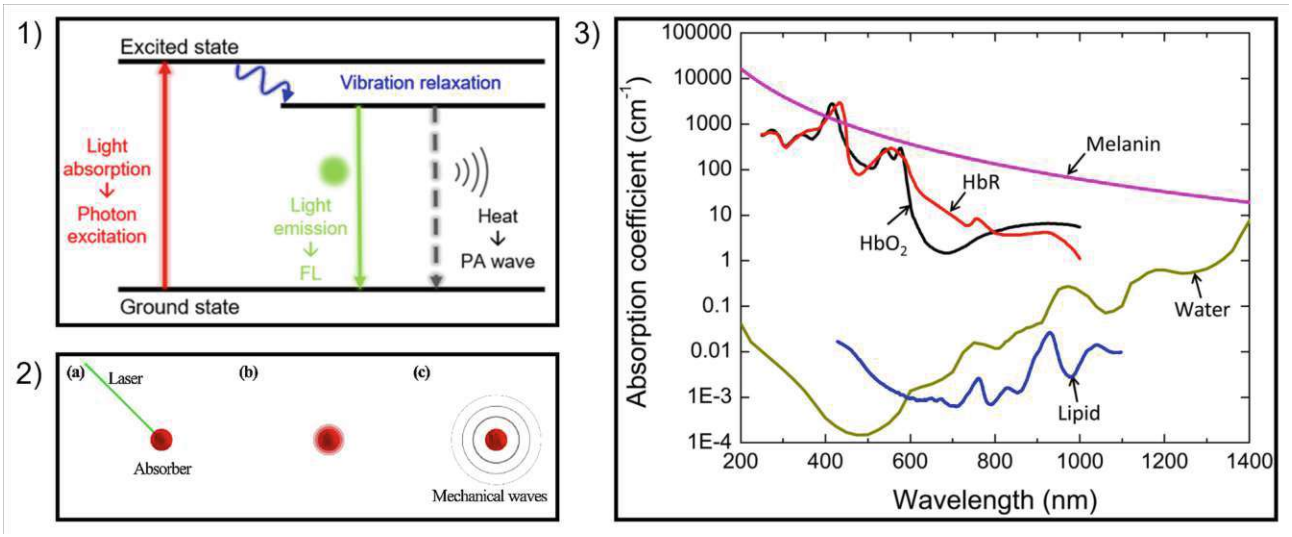


**Figure 1.** 1) Schematic energy diagram of principle of signal generation through light absorption [28] 2) schematic illustration of the photoacoustic effect [29] 3) various absorption coefficient spectra of endogenous tissue chromophores [30]

## 2.2 Tissue-mimicking Phantoms for Optoacoustic Imaging

Phantoms for optoacoustic imaging systems are artificial test objects designed with controlled geometries and material composition to replicate tissue characteristics as well as the propagation and interaction of light and acoustic waves within biological tissues. [31] As optoacoustic imaging is a hybrid modality combining ultrasound and optical imaging, it is essential for the acoustic and optical properties of phantoms to be independently adjustable, allowing for a broad range of simulated tissue characteristics. This makes the development and characterization of standard phantoms particularly challenging. Hacker et al. [6] provided a detailed list of the physical properties that influence image quality in optoacoustic imaging (Table 1).

| Type | Parameter | Symbol | Unit | Description |
|---|---|---|---|---|
| Optical | Optical absorption coefficient | $\mu_a$ | $m^{-1}$ | quantifies how much light a material absorbs per unit distance |
| | Refractive index | $n$ | - | measures how much light slows down in a medium compared to vacuum |
| | Anisotropy factor | $g$ | - | quantifies the degree of directional dependence of scattering in a medium |
| | Reduced scattering coefficient | $\mu_{s'}$ | $m^{-1}$ | quantifies light scattering in a medium, accounting for anisotropy |
| Acoustic | Acoustic attenuation coefficient | $\alpha$ | $dB/m$ | measures the decrease in sound intensity per unit distance |
| | Speed of sound | $c$ | $m/s$ | rate at which sound waves travel through a medium |
| | Back-scattering coefficient | $\mu_{bs}$ | $m^{-1}$ | quantifies the fraction of scattered light that is redirected back towards the source |
| Mechanical | Density | $\rho$ | $kg/m^3$ | mass per unit volume of a substance |
| | Young's Modulus | $E$ | $N/m^2$ | measures a material's stiffness or elasticity under stress |
| Thermoelastic | Grueneisen parameter | $\Gamma$ | - | relates volume changes to energy changes in a material |

**Table 1.** Definition of the essential material properties for optical and acoustical imaging applications [6]

Various types of tissue-mimicking materials have been investigated as phantom test objects. They can be divided into water-based and oil-based materials. Water-based materials like gelatin and agarose are among the most popular tissue-mimicking materials, due to their easy accessibility, simple preparation affordability and reliable replication of human tissue characteristics. [8] However, their main drawbacks include rapid degradation due to bacterial growth and dehydration, which limits their stability over time, along with a high susceptibility to physical damage. [8] Polyvinyl alcohol (PVA), an additional water-based material, has greater longevity and structural rigidity compared to hydro-gels, but requires extensive preparation including freeze-thaw cycles lasting several days and may be sensitive to humidity. [32]

Oil-based tissue-mimicking materials are particularly beneficial for creating phantoms with strong temporal stability due to their resistance to dehydration. Common example materials for optical imaging include polyester resin, epoxy resin and silicone, although these materials

generally lack suitable acoustic properties for optoacoustic applications. [33] Cabrelli et al. [8] introduced styrene-ethylene/butylene-styrene (SEBS) copolymer gels as promising, easy-to-manufacture tissue-mimicking materials that offer long-term stability for various optical imaging modalities in multi-modal applications. However, in that study the optical absorption and scattering coefficients were not independently tuned and the values were lower that those for typical soft tissue. [33] Polyvinyl chloride plastisol (PVCP) is an oil-based material that can mimic both acoustic and optical properties. [34] Although it is stable and relatively easy to obtain, it yet has to be fully exploited as a phantom material for optoacoustic imaging. [32] Commercial gel wax is an oil-based material that effectively mimics both acoustic and optical properties and has been utilized in numerous studies. [33, 35–38] Similar to commercial PVCP, the batch-to-batch consistency of commercial gel wax is not well-documented, which may lead to variations in the acoustic and optical properties of phantoms produced using the same manufacturing methods. [39] Despite this, gel wax phantoms are gaining interest due to their ease and speed of production, non-toxic composition, ability to be cast into anatomically realistic shapes and cost-effectiveness. [40]

Phantoms are an important tool used in the development and optimisation of imaging systems or algorithms, by providing a more clinically realistic imaging environment. Other applications of phantoms include system inter-comparison, benchmarking, clinical training, clinical trial standardization, recalibration and quality assurance. [7]

Tissue-simulating phantoms have been integrated into international performance standards for imaging technologies including magnetic resonance imaging, X-ray, computed tomography and ultrasound. Despite substantial efforts to create standardized phantoms for photogenic imaging systems, there is no accepted standard physical phantom available for optoacoustic imaging. [32]

Using standardized and controlled materials allows for improved regulation of acoustic and optical properties. A standardized manufacturing process encompasses factors such as heating temperature and duration, component ratios and the application and timing of vacuum and ultrasonic equipment, in addition to the materials utilized. [39] By establishing the International Photoacoustic Standardization Consortium (IPASC) [41] in 2021, there has been a shift towards standardization issues in optoacoustic imaging and related technologies. [6]

# 3 Materials and Methods

## 3.1 Measuring System and Measuring Software

### 3.1.1 MSOT Acuity Echo

The MSOT Acuity Echo (Figure 2) is composed of three primary components which are an acquisition unit, a hand-held probe and a user interface.


**Figure 2.** MSOT Acuity Echo system [10]

The 290 $kg$ MSOT Acuity Echo has dimensions of 1.96 $m$ x 0.78 $m$ x 1.1 $m$. It includes a power supply, a signal-generating laser, a data acquisition unit for imaging and a PC equipped with system software for data processing. The Class 4 pulse-generating laser operates in two wavelength configurations, both within the near infra-red range. Type 1 covers wavelengths from 680 $nm$ to 980 $nm$ and 1064 $nm$, while Type 2 allows for wavelengths between 660 $nm$ and 1300 $nm$. The pulse repetition rate is adjustable from 10 $Hz$ to 25 $Hz$, with pulse duration ranging from 4 $ns$ to 10 $ns$.

The user interface, which includes a monitor and keyboard, can be adjusted using the monitor arm. For safety, a laser foot pedal must be pressed to activate the laser.

### 3.1.2 MSOT Acuity Echo Probe

The hand-held probe measures 56 $mm$ x 143 $mm$ x 121 $mm$ and has a 2.9 $m$ cable. It is stored in a holder attached to the MSOT Acuity Echo. For image acquisition, a fibre bundle within the probe directs laser radiation toward the center of the imaging area. Ultrasound

waves generated by the imaging target are detected by the probe's arc-shaped 2D ultrasound transducer array, featuring 256 detector elements arranged with a 125° coverage and a center frequency of 4 $MHz$.


**Figure 3.** left: Hand-held probe for 2D image acquisition; middle: Field of view generation, right: 3D model of the MSOT Acuity Echo hand-held probe with 125° coverage and 256 transducer array elements (image sourced from iThera Medical presentations)

The coupling medium within the hand-held probe (heavy water) ensures effective signal detection. The resolution depth at the lateral center of the image is 10 $mm$ ($\pm$ 5 $mm$). Resolution in the $x$- and $y$-direction is $< 1$ $mm$ ($\pm$ 2 $mm$) and 2.5 $mm$ ($\pm$ 2 $mm$) in $z$-direction, as specified for breast and abdominal tissue in the user manual.

### 3.1.3 viewMSOT

The MSOT Acuity's software, viewMSOT (Figure 4), offers a graphical user interface for acquiring, displaying and analysing multi-spectral optoacoustic images. It also includes tools for managing patient data, exporting images and generating reports.

Since image analysis was conducted externally using Python, the primary functionality utilized was the examination screen. This feature facilitated the visualization and recording of MSOT data in various live modes, including single- and multi-wavelength configurations, with or without accompanying ultrasound images. Furthermore, it provided control over imaging parameters and supported the viewing, freezing and recording of snapshots or image sequences.

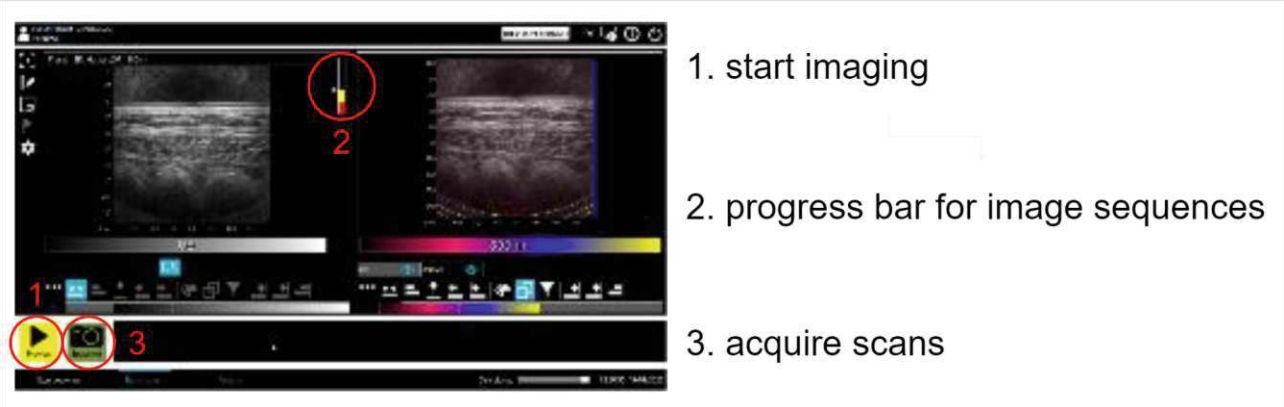


**Figure 4.** viewMSOT's examination screen

## 3.2 Measurement Objects and their Manufacturing Process

### 3.2.1 Zerdine Phantom

To provide calibration phantoms along with the device to customers, Zerdine hydro-gel-based phantoms were ordered from CIRS (Figure 5). The properties specified by CIRS are presented in Table 2.


**Figure 5.** Schematic image showing the desired dimensions for the Zerdine phantom order; Positioning of the probe holder on the the Zerdine phantom casing (images on the left and right are sourced from iThera Medical presentations)

The casing and probe holder were designed so that the center of the field of view could be positioned over each of the three embedded inclusions. The material of the first layer membrane is Teflon, while the second layer is made of polyethylene (PE). The ink concentrations for the inclusions #1, #2, #3 are 0.05%, 0.025% and 0.005% by volume.

| | |
|---|---|
| speed of sound (base material) | 1531 $m/s$ |
| speed of sound (absorbers) | 1531 $m/s$ |
| attenuation (base material) | 0.17 $dB/cm/MHz$ |

**Table 2.** Specified properties of the Zerdine phantoms by CIRS

### 3.2.2 Gel Wax Phantom

Building upon the 2018 study by Maneas et al. [33], which introduced gel wax, a commercially available, cost-effective, non-toxic and optically transparent mineral oil-based material, as a potential tissue-mimicking material for optoacoustic imaging, the objective was to develop an in-house phantom utilizing this material.

Similar to Bohndiek et al. [32], the following design constraints were established for a gel wax prototype phantom:

a) To maintain consistent acoustic, mechanical and thermoelastic properties within the phantom, the absorbers and the matrix should be made from the same material [42, 43].

b) The absorbers should have a defined shape, size and position, with optical absorption representative of biological tissue in the near infra-red wavelength range of 680 $nm$ - 950 $nm$ [44–46].

c) The optical properties of the background matrix containing the absorbers should be adjustable.

d) The phantom should provide a stable signal over time, be insensitive to physical influences or bacterial contamination and also be easy to manufacture and handle.

The completion of this task involved utilizing a chemistry laboratory for the production of the phantoms, a 3D printer for fabricating the phantom casing and a laser laboratory equipped with the MSOT Acuity Echo imaging device for scanning the phantoms. A photo-spectrometer was employed to evaluate the absorbing properties of the phantom matrix and the absorbers. However, the evaluation of scattering properties was constrained by the unavailability of more precise methods, such as an integrating sphere, within the time frame of this work. As a result, the analysis relied solely on the capabilities of the photo-spectrometer.

**Utility preparations**
The tools used during the manufacturing process were:

- A magnetic heating plate with magnetic stirrers was used to ensure homogeneous mixing of the phantom material.
- To achieve an even distribution of the additives, free from aggregates, sedimentation or air bubbles, a sonicator and vacuum pump were employed.
- A photo-spectrometer was used to assess the absorbance of the sample materials.

To ensure smooth operation during the manufacturing process, several preparations were made in advance:

- The sonicator was filled with distilled water and preheated to the maximum temperature (T = 60°C).
- The magnetic heating plate, with a pan containing cooking oil, was preheated to T = 180°C.
- The required ingredients (gel wax, $TiO_2$ and oil-based ink) were weighted.
- Beakers (120/500 $mL$) and the phantom casing were prepared.
- For the production of gel wax-based absorbers, a Teflon tube was connected to a vacuum pump. A filter was placed between the tube and the pump to prevent gel wax material from entering the pump.

**Gel wax matrix**
Since gel wax is primarily composed of oil, it degrades at high temperatures. To prevent unnecessary heating while ensuring uniform distribution of $TiO_2$ in the mixture, a small amount (20 $g$) of clear gel wax (cGW) was used for dissolving the $TiO_2$. The gel wax was placed in a 120 $mL$ beaker and set into the pre-heated pan containing oil at 180°C. After 5 minutes, the gel wax melted, allowing the $TiO_2$ to be added. The magnetic stirrer was set to its maximum speed, ensuring the solution didn't splash. The mixture was stirred under heat for 30 minutes. To achieve a uniform distribution of $TiO_2$, free from aggregates or sedimentation, the mixture was sonicated for 2 minutes to improve results. This process was repeated three times and then the beaker was placed under vacuum to remove air bubbles. Once cured in the beaker,

the resulting mixture solidified into a pallet, creating a high-concentration scattering gel wax pallet (hcsGWp).

The hcsGWp could either be stored or used immediately to continue the production of the scattering gel wax (sGW) stock solution. The target amount for the sGW was 409 $g$. To achieve this, the remaining 389 $g$ of cGW was placed into a beaker and melted for 20 minutes. The hcsGWp was then added to the beaker and the magnetic stirrer was again set to its maximum rotation speed, ensuring the solution didn't splash. The mixture was stirred for 10 minutes, sonicated and degassed to improve the results. The manufacturing process for the sGW stock solution is shown in Figure 6.

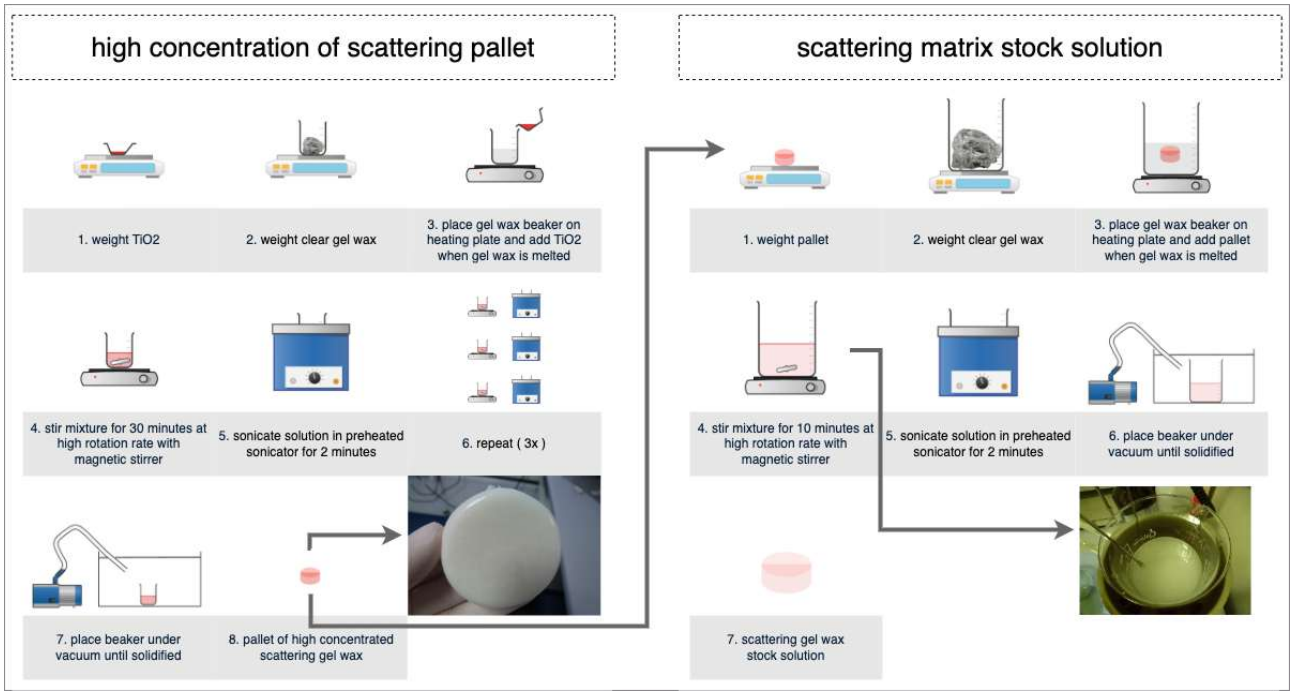


**Figure 6.** Manufacturing process of the scattering gel wax (sGW) stock solution (schematic representations of lab equipment sourced from Chemix)

### Gel wax absorbers

To manufacture gel wax-based absorbers, an absorbing-scattering gel wax (asGW) stock solution had to be prepared first. The process for creating asGW was identical to the production of sGW, as described in the previous paragraph, with the key difference being the use of sGW instead of cGW and the substitution of $TiO_2$ with oil-based ink as the ingredient. This results in the production of a high-concentration absorbing-scattering gel wax pallet (hcasGWp), which was then mixed with sGW to create a batch of asGW. To produce smaller batches of varying absorbance for inclusion preparation, different amounts of asGW were weighed and diluted with a larger amount of sGW by melting the gel wax mixture in a beaker on a heated magnetic stir plate for 10 minutes. The resulting absorbing-scattering gel wax inclusion amounts (asGWia) were poured into cuvettes and analysed using the photo-spectrometer.

The manufacturing process for gel wax-based absorbers, shown in Figure 7, began with filling various asGWia solutions into tubes. This was done by placing a Teflon tube with an inner

diameter of 2 $mm$ into the beaker containing the melted asGWia solution, where the mixture was vacuumed into the tube. The solution temperature should be approximately 80-90°$C$ for optimal results. This temperature range provides a good balance between viscosity and minimal air bubble formation. To prevent bubbles, it was advisable to vacuum shorter tube sections by starting the vacuum pump and turning it off immediately. These sections were then cut into 5 $cm$ pieces, from which the gel wax was extracted. To avoid flattening the cylindrical absorbers, they were temporarily stored on a plate in a bridge-like formation. Since these 2 $mm$ thin absorbers were very fragile and would easily deform when embedded in the hot matrix during the molding process, a coating method was developed. To produce these coatings, 50 $g$ of sGW was prepared to serve as a dip solution. Based on thermodynamic principle, a greater temperature gradient speeds up the cooling process, so the inclusions were first placed in a freezer before being dipped into the sGW solution at 80-90°$C$. Immediately after being dipped in the sGW solution, the inclusion was immersed in cooled water to promote rapid hardening. This quick cooling method ensured that the inclusion layers have a consistent thickness. To achieve a 3 $mm$ layer, this process was repeated five times. Before each new layer was applied, the inclusion was placed in the freezer, set to -20°$C$, for 3 to 4 minutes.

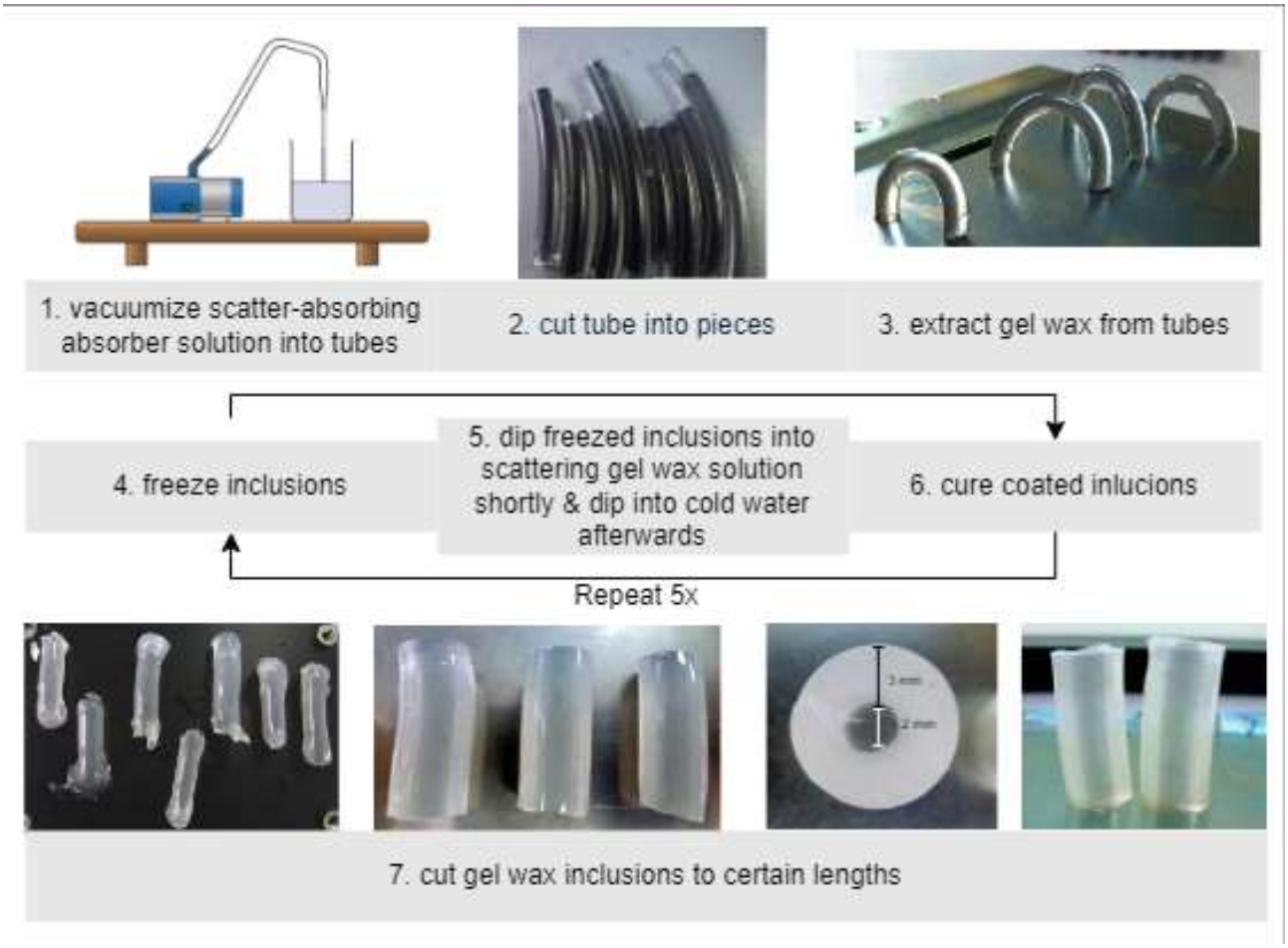


**Figure 7.** Manufacturing process of the coated gel wax absorbers (schematic representations of lab equipment sourced from Chemix)

### Molding process

The sGW solution for the phantom's background was heated and molded into the phantom mold at a temperature of 100°C. After allowing the sGW to cure for one hour, it was removed, flipped and placed back into the mold upside down. This revealed three half-cylindrical inner shapes at the top. The coated absorbers were then placed into these shapes and the mold was filled to the top with sGW (Figure 8).

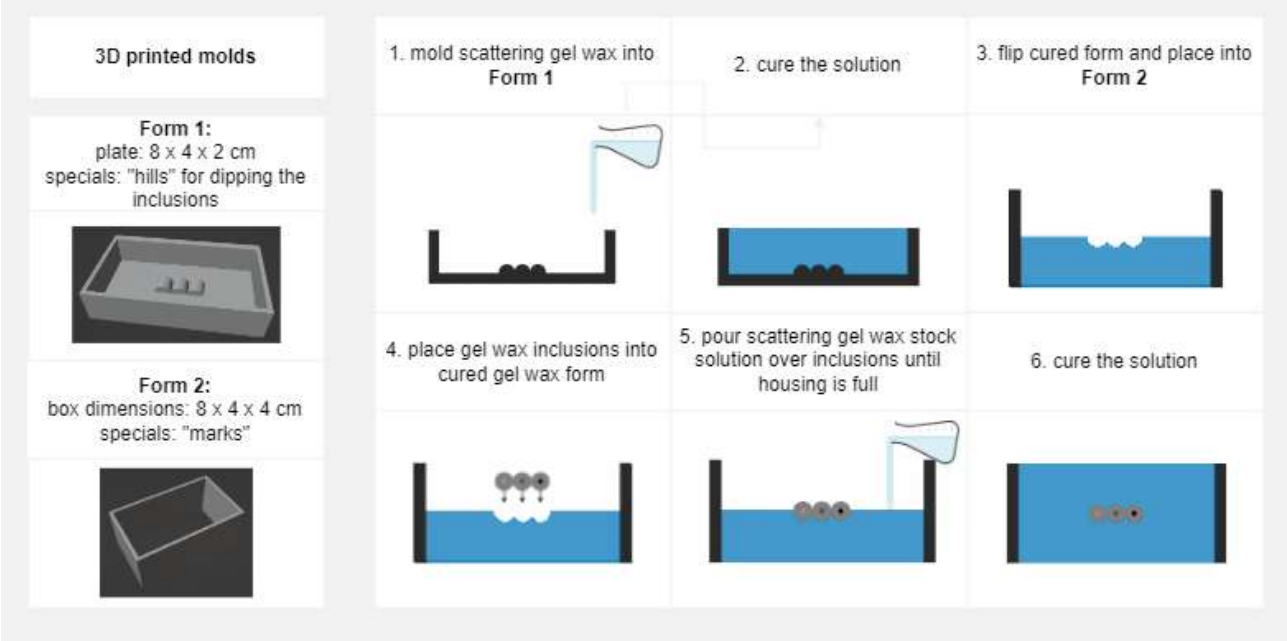


**Figure 8.** Molding process of the gel wax phantom using in-house 3D-printed molds (schematic representations of lab equipment sourced from Chemix)

The schematic images of the 3D-printed molds used are shown in Figure 8, although in reality, the mold had rounded edges. The molding form for the phantom block was designed and manufactured in-house and consists of two parts: a box without a top or bottom plate and a box with a plate with three bulges. In the past, the 3D printing material poly-methyl methacrylate (PMMA) has proven effective as a mold for materials with high temperatures up to 200°C. The 3D printer used was of the VAT polymerization type, where the printed photopolymer resin was hardened by exposure to a light source.

Inspired by the Zerdine phantom, the prototype of the gel wax phantom featured a similar design. It consisted of three different scatter-absorbing inclusions placed inside of a phantom casing (Figure 9).


**Figure 9.** Gel wax phantom prototype (the image 'phantom inside' was captured by colleagues at iThera Medical following the conclusion of the project period)

## 3.3 Data Collection

### 3.3.1 Site and System Configuration

The acquisition process (Figure 10) started by turning on the device and cleaning the hand-held probe. To ensure the expected image quality, a laser self-test checked that the laser energy was within the required range. For safe laser operation, safety goggles had to be worn. Additional safety was provided by a foot pedal, which had to be pressed to activate the laser and an acoustic signal was emitted when the laser was in operation. Depending on the application, the appropriate preset was selected. The preset was an .xml file that defined general settings (e.g. preset name, detector used for image acquisition), processing settings (e.g. reconstruction parameters like filter type, high-pass and low-pass cut-off frequency in $Hz$, frame rate, depth correction, speed of sound) and experimental settings (e.g. preview settings, averaging settings, illumination range for acquisition). When a new imaging session began, the acquired images were saved to the corresponding database session. For research purpose, the acquired data was transmitted to a Windows File Sharing folder using the Remote Data Access Port.

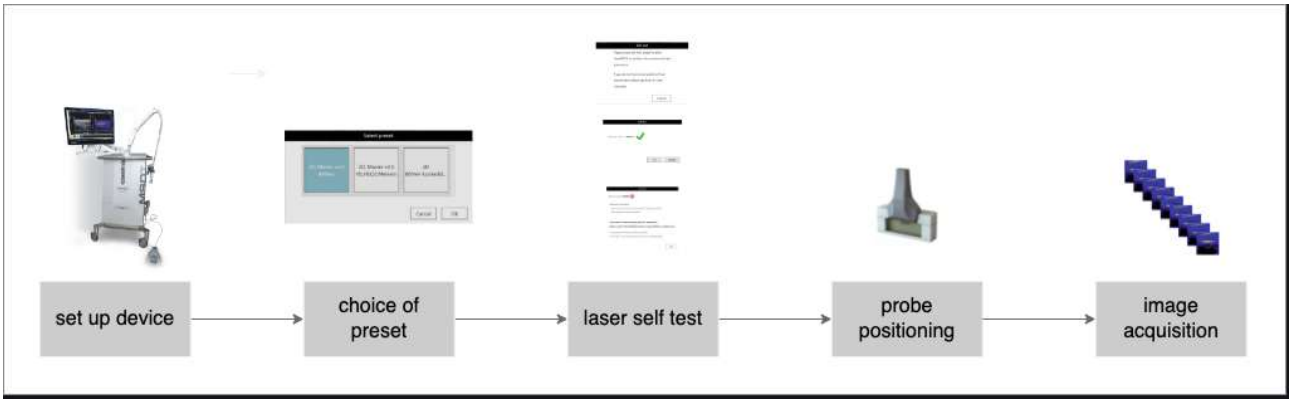


**Figure 10.** Schematic image of the acquisition process steps

The storage structure for the captured images (Figure 11) was organized such that the data set from each imaging session was saved in a folder labeled 'Study_<X>', where $X$ represents the consecutive session number. Within these folders, the acquired scans were stored in corresponding 'Scan_<Y>' folders, with $Y$ indicating the consecutive number of each captured image.

A scan folder contained following files:

- <random string>.jpg: A reconstructed image generated by viewMSOT, using the processing settings defined in the preset, exported as a .jpeg file.
- Scan_<Y>.msot: The captured signals detected by each transducer element got stored in the corresponding Scan_<Y>.msot file. This file served as a container for multiple images acquired across the illumination range and sweep number as defined in the preset. Additionally, an internal energy meter monitored the energy of each laser pulse to track any fluctuations, with this data also saved within the .msot file.
- Scan_<Y>.bin, Scan_<Y>.img, Scan_<Y>.irf: The remaining files were generated by viewMSOT for reconstruction.

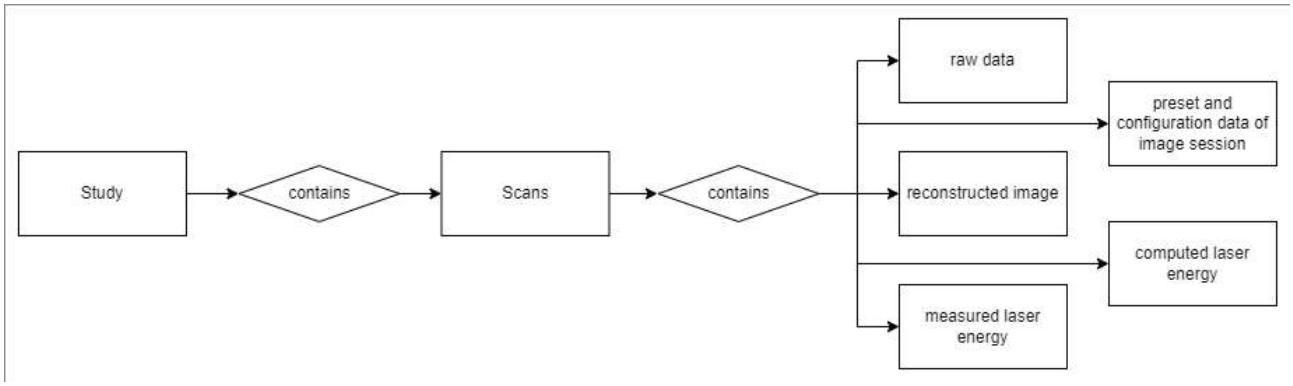


**Figure 11.** Organization of the acquired scan data

### 3.3.2 Generated Studies and their Research Questions

Several studies have been conducted, with those selected for evaluation presented in Table 3 and Figure 12. Table 3 provides a detailed summary of the phantom composition, the number of scans performed at each wavelength, the absorbers analysed and the corresponding scan dates for each study. Figure 12 displays the acquired images for each absorber in the studies: the upper images were automatically generated using viewMSOT, while the lower images represent reconstructed and processed 3D images, with the reconstruction methodology elaborated upon in the subsequent chapter.

| Study | Phantom composition | Number of scans per wavelength | Number of absorbers | Scan date |
|---|---|---|---|---|
| Study 1 | Zerdine | 60 | 3 | 2018-08-08 |
| Study 2 | Zerdine | 60 | 3 | 2018-08-13 |
| Study 3 | Zerdine | 60 | 3 | 2018-08-17 |
| Study 4 | Zerdine | 60 | 3 | 2018-08-23 |
| Study 9 | gel wax inclusions without $TiO_2$ coating | 21 | 7 | 2018-12-03 |
| Study 10 | gel wax inclusions with $TiO_2$ coating | 21 | 7 | 2018-12-19 |

**Table 3.** Overview of the studies discussed

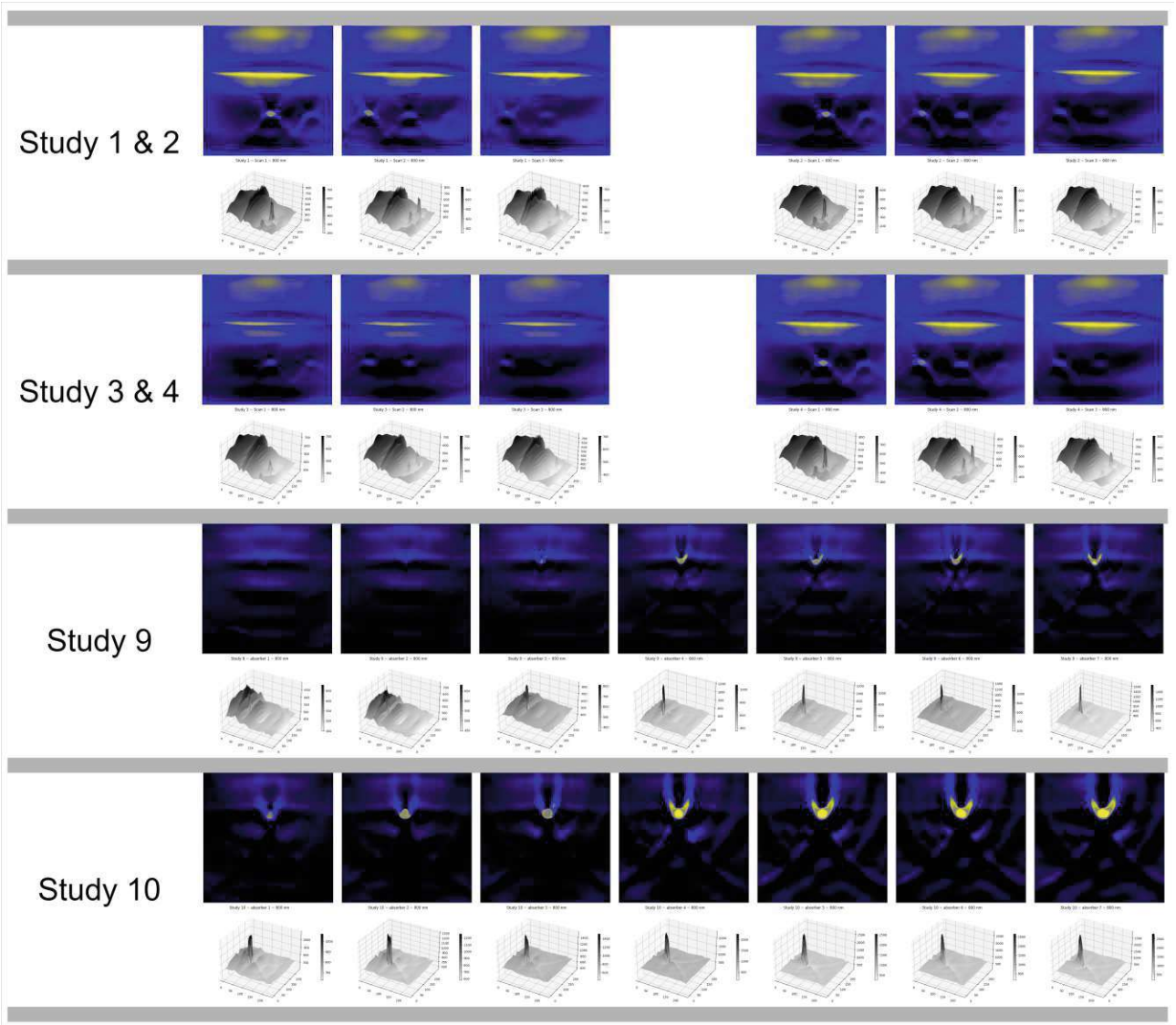


**Figure 12.** Generated studies with examples of acquired images

The following questions were identified for analysis and discussion:

- How stable is the laser energy throughout the study sessions?
- How does the offset, an artefact of image reconstruction, vary with absorber intensity?
- What is the absorber signal variability throughout the study sessions?
- What is the non-absorber signal variability throughout the study sessions?
- How does the number of averaged images affect signal variability?
- How does the sensitivity field of the detector vary when comparing the signal at the center to the signal at the outer edges of the field of view?
- How does the illumination wavelength influence the results of the above questions?
- How reproducible is the automated positioning of the ROIs?

## 3.4 Data Processing and Data Analysis

Multiple data types required quantification. For each data type, customized processing and quantification codes were developed.

The processing stages were as follows:

- Laser energy readout
- Image reconstruction
- Offset adjustment of the reconstructed images
- Averaging of the offset-adjusted images
- Evaluation of the center coordinate positions
- ROI extraction

The parameters used for quantification were:

- Laser energy
- Offset
- Extracted ROI values
- Center coordinate positions
- Optical density of gel wax samples

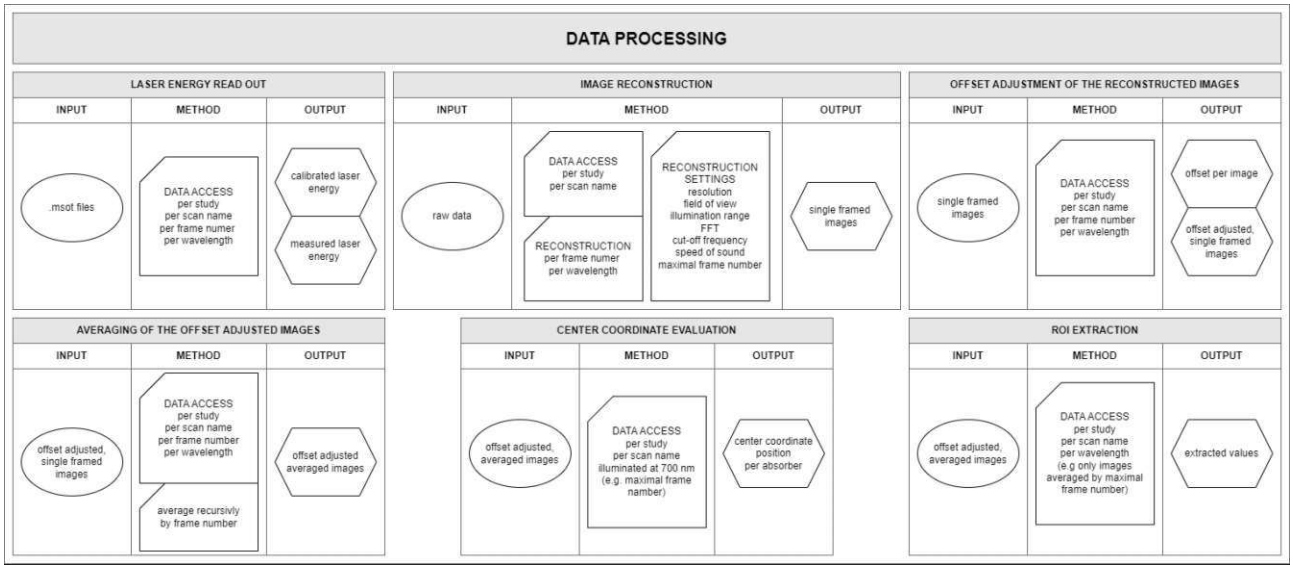


**Figure 13.** Overview of processing stages

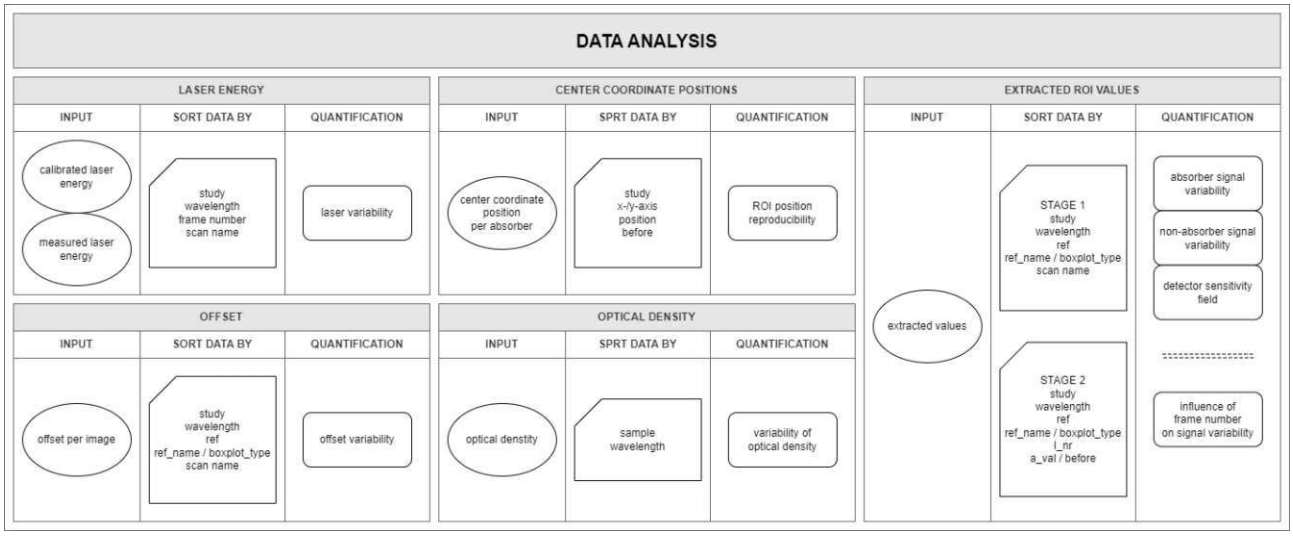


**Figure 14.** Overview of parameters for quantification

### 3.4.1 Laser Energy

The algorithm read the .msot files by scan folder and extracted the measured and calibrated laser pulse energy saved in the xml structured file. This two variables were exported as .csv files for the quantification of the stability of the laser energy throughout the study sessions.

### 3.4.2 Image Reconstruction

The reconstruction package *iLib*, developed in Python by iThera Medical, was utilized for image processing. Upon selecting a study, the relevant .msot files within each scan folder were accessed.

A multi-spectral scan contains multiple images. The raw MSOT data from a single scan was sequentially accessed and reconstructed based on frame number and wavelength. Each reconstructed image was saved as an individual text file for subsequent analysis.

Figure 8 provides a schematic representation of the reconstruction process for a single MSOT file (depicted as a white cylindrical object), resulting in a series of text files (represented as light gray rectangles). The total number of images generated from a single MSOT file corresponds to the product of the number of frames and the number of illumination wavelengths specified in the preset configuration.

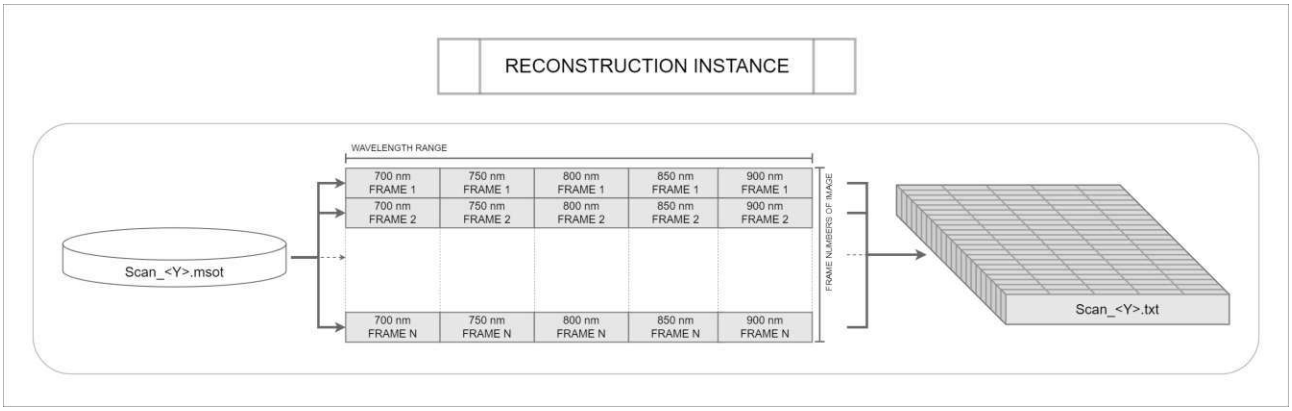


**Figure 15.** Schematic of the reconstruction process of a single MSOT file, resulting in a collection of text files

To initialize the reconstruction algorithm, default settings were applied. Table 4 and Table 5 provide a summary of the parameters used in the reconstruction process.

| **Description** | **Parameter values** |
|---|---|
| resolution of the reconstructed images | 0.15 $mm$ in x and y direction (default settings) |
| field of view | 35 $mm$ in x and y direction (default settings) |
| illumination range defined in the preset | 700 $nm$, 730 $nm$, 750 $nm$, 760 $nm$, 800 $nm$, 850 $nm$, 900 $nm$ |
| FFT | FFT on signal and phase flip for the impulse response (default settings) |
| cut-off frequency | 50 $kHz$ - 6 $MHz$ (default settings) |

**Table 4.** General reconstruction settings

| Study | Imaging target material | speed of sound $[m/s]$ | maximal frame number |
|---|---|---|---|
| Study 1 | Zerdine | 1520 | 25 |
| Study 2 | Zerdine | 1520 | 25 |
| Study 3 | Zerdine | 1520 | 25 |
| Study 4 | Zerdine | 1520 | 25 |
| Study 9 | gel wax | 1475 | 25 |
| Study 10 | gel wax | 1475 | 25 |

**Table 5.** Study specific reconstruction settings

### 3.4.3 Offset Adjustment of the Reconstructed Images

The reconstructed images contained negative pixel values, considered artefacts from the reconstruction process, referred to as offsets. To avoid quantification errors arising from these negative values, all pixel values in the images were shifted by the minimum offset value identified within each study. This method ensured that the relative ratios of pixel values were preserved across the study. The offset values were exported as .csv files to facilitate quantification and analysis across study sessions.

### 3.4.4 ROI Extraction Including Center Coordinate Evaluation

The signal extraction process included two main steps: Step 1 identified the centroid coordinates of each absorber per scan by analysing noise-reduced, averaged images at a single wavelength. In Step 2, single-frame images were accessed across various wavelengths and frame numbers, using the determined coordinates, identified in Step 1, to extract the ROIs.

Figure 16 and Figure 17 illustrate the intermediate results of both steps in detail.

In the first step of the extraction algorithm, only images captured at 700 $nm$ were utilized. The absorber's position was assumed to remain consistent across all frames and wavelengths within the same scan. To reduce image noise, each scan was averaged across the maximum frame number. Initial ROIs were defined around each absorber. These regions were then cropped and binary thresholded. The contour of the thresholded image was analysed and their center was calculated. The centroid coordinates were derived based on the initial coordinates, cropped ROI size and the final ROI dimensions. The centroid coordinates were then exported as a .csv file of each study, corresponding to the scan number and absorber position.

In the second step, each image was accessed according to frame number and illumination wavelength. The .csv file from the first step was imported and the final ROIs were cropped at the respective positions. The pixel values within each ROI were averaged and these averaged ROI values were then exported along with the associated scan number, frame number, wavelength and absorber position.

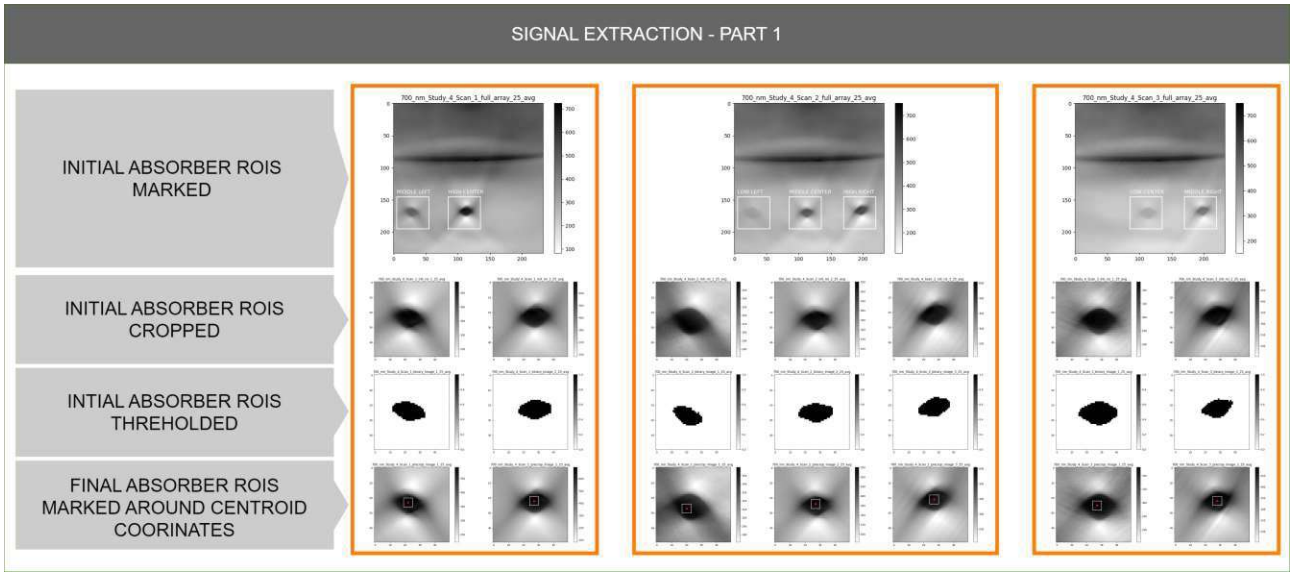


**Figure 16.** First step of signal extraction algorithm

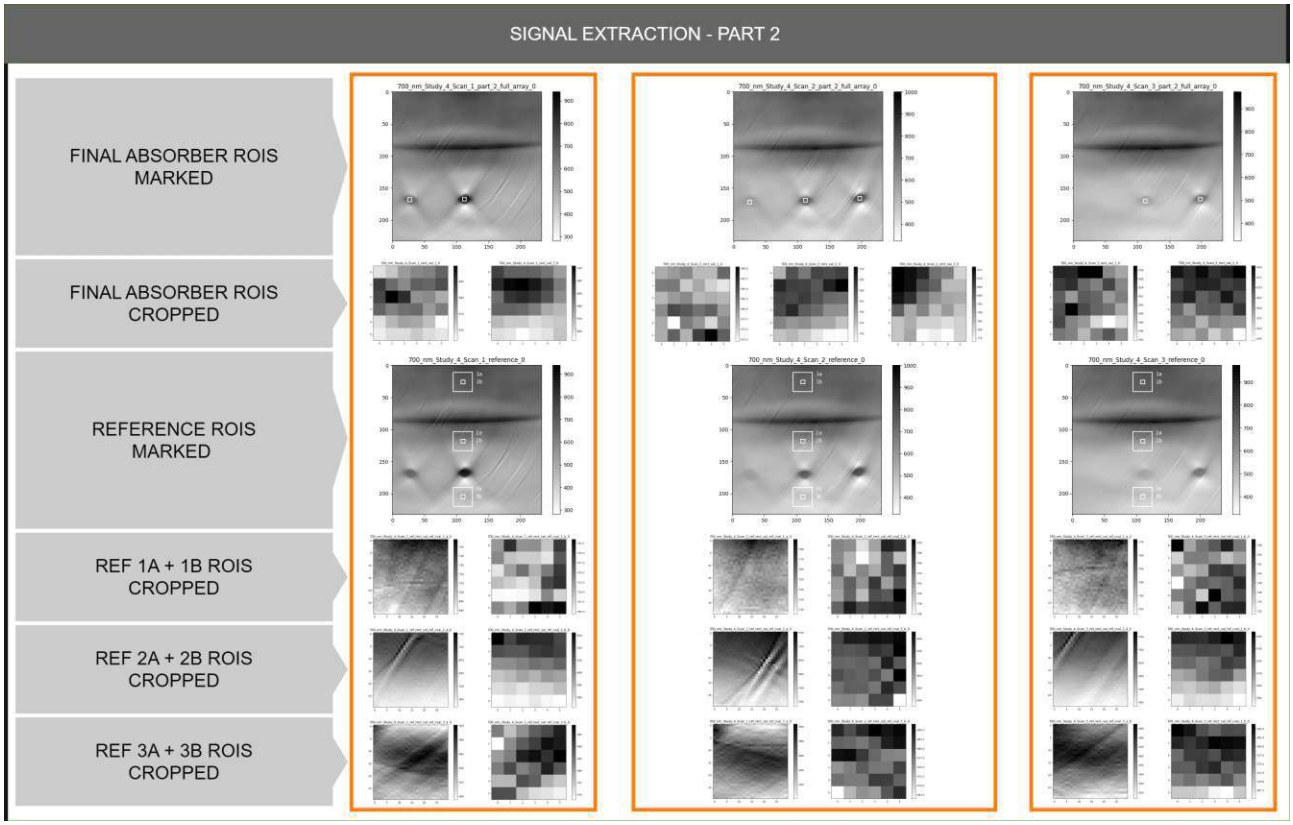


**Figure 17.** Second step of signal extraction algorithm

In addition to the centroid coordinates, a set of non-absorber ROIs was also extracted. These coordinates remain consistent across all scans within a study, as illustrated in Figure 18.

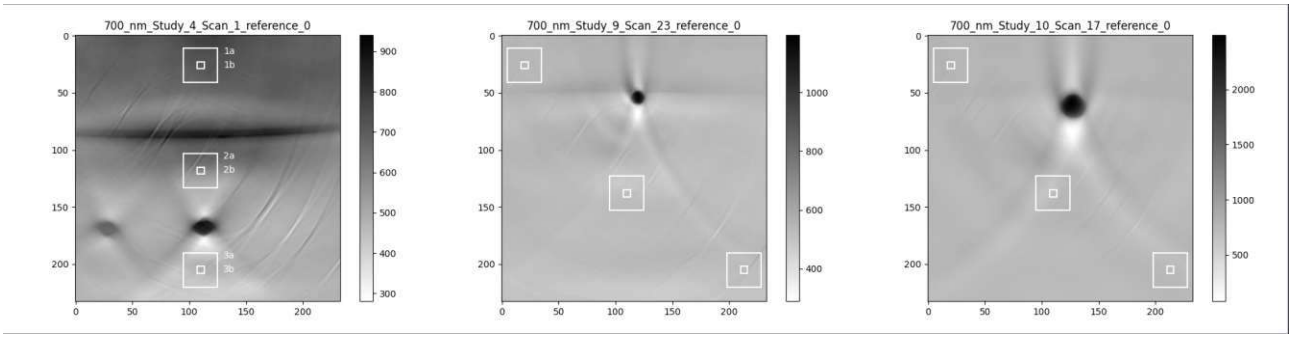


**Figure 18.** Set of ROIs of non-absorber signal

### 3.4.5 Assessment of the Optical Characteristics of Gel Wax Samples

The photo-spectrometer was used to evaluate the absorbance of the sample cuvettes. Absorbance is a measure of the amount of light absorbed by a sample when following the Beer-Lambert Law

$$\boxed{I = I_0 \cdot e^{-\mu_a \cdot d}} \tag{3}$$

where $I_0$ is the incident intensity, $I$ the transmittance intensity, $\mu_a$ the absorption coefficient and $d$ the thickness of the sample, and a logarithmic ratio of the intensity of the light entering the sample to the intensity of the light that passes through:

$$A = log\left(\frac{I_0}{I}\right) \tag{4}$$

The dimension of the sample cuvettes used were of 1 $cm$ x 1 $cm$ x 3 $cm$. The evaluation spectrum was set according to the wavelengths in the near infra-red range from 700 $nm$ to 900 $nm$ at 50-$nm$ steps. Since the samples where not purely liquid, the measured parameter should be correctly called optical density ($OD$), referring to the attenuation of light, which includes both absorption and scattering of light. Absorbance and optical density were treated as equivalent, as they are determined using the same measurement technique.

The absorption coefficient $\mu_a$ can be determined from the $OD$ by some equation conversions starting with

$$\frac{I}{I_0} = e^{-\mu_a \cdot d} \tag{5}$$

$$ln\left(\frac{I}{I_0}\right) = -\mu_a \cdot d \tag{6}$$

$$ln\left(\frac{I_0}{I}\right) = \mu_a \cdot d \tag{7}$$

and $ln(x) = log_{10}(x) \cdot 2.304$

$$ln\left(\frac{I_0}{I}\right) = log_{10}\left(\frac{I_0}{I}\right) \cdot 2.304 = \mu_a \cdot d \tag{8}$$

and Equation 4

$$OD \cdot 2.304 = \mu_a \cdot d \tag{9}$$

resulting in

$$\boxed{\mu_a = \frac{OD \cdot 2.304}{d}} \tag{10}$$

The scattering coefficient ($\mu_s$) of the scattering material could not be evaluated due to the absence of technology such as the Double Integrated Sphere utilized in Maneas et al. [33] The optical density ($OD$) of the scattering material was measured with the assumption that its properties would remain consistent provided the preparation process remains unchanged.

# 4 Results and Interpretation

## 4.1 Terminology and Definitions

To analyse the mean, standard deviation and percentage error, the ROI values were grouped according to various properties (Table 6).

| Name | Definition | Values | Use case |
|---|---|---|---|
| cval | averaged pixel values of ROI | - | general |
| phantom | imaging target material | Zerdine, gel wax | general |
| study | study | Study 1, Study 2, Study 3, Study 4, Study 9, Study 10 | general |
| wlg | illumination wavelength | 700 $nm$, 730 $nm$, 750 $nm$, 760 $nm$, 800 $nm$, 850 $nm$, 900 $nm$ | general |
| averaged | boolean value | 'True' if averaged by frame numbers else 'False' | general |
| frame_nr | frame number <x> | 'single' if averaged = False, else 'averaged by <x> frame numbers' | general |
| scan_name | folder name of scan data | scan number | general |
| ref | boolean value | 'True' if non-absorber ROI, 'False' if absorber ROI | general |
| ref_name | corresponding ROI position of non-absorber ROI | 1a, 1b, 2a, 2b, 3a, 3b | general |
| before | boolean value | 'True' if scan number <30 else 'False' | Zerdine specific |
| I_nr | inclusion index in center of field of view | 1 = HIGH, 2 = MEDIUM, 3 = LOW | Zerdine specific |
| absorber | corresponding absorber of cval | HIGH, MEDIUM, LOW | Zerdine specific |
| position | corresponding position of cval | LEFT, CENTER, RIGHT | Zerdine specific |
| boxplot_type | f'{absorber} {position}' | various combinations | Zerdine specific |
| label | f'{boxplot_type} {wlg}' | various combinations | Zerdine specific |
| a_val | absorber index of loose inclusion | 1-7 / 1-10 | gel wax specific |

**Table 6.** Nomenclature for image data analysis

## 4.2 Laser Pulse Energy Quantification

To assess the variability in system performance, this chapter examines the stability of laser pulse energy, both within individual studies and across multiple study sessions. Data acquisition and

processing are described in 3.4 Data Processing and Data Analysis.

The raw data indicates that LASER-CALIBRATION-FILES from different dates were used across the studies (Table 7).

| | |
|---|---|
| Study 1, 2, 4 | 2018-08-02 |
| Study 3 | 2018-08-14 |
| Study 9, 10 | 2018-10-05 |

**Table 7.** Dates of laser calibration files used across study sessions

Figure 19 shows the laser pulse energies in $mJ$ as a function of wavelength and the corresponding percentage errors for studies 1-4, 9 and 10. The red line represents the laser pulse energies as computed (calibrated) by viewMSOT, while the box-plots represent the measured laser pulse energies.

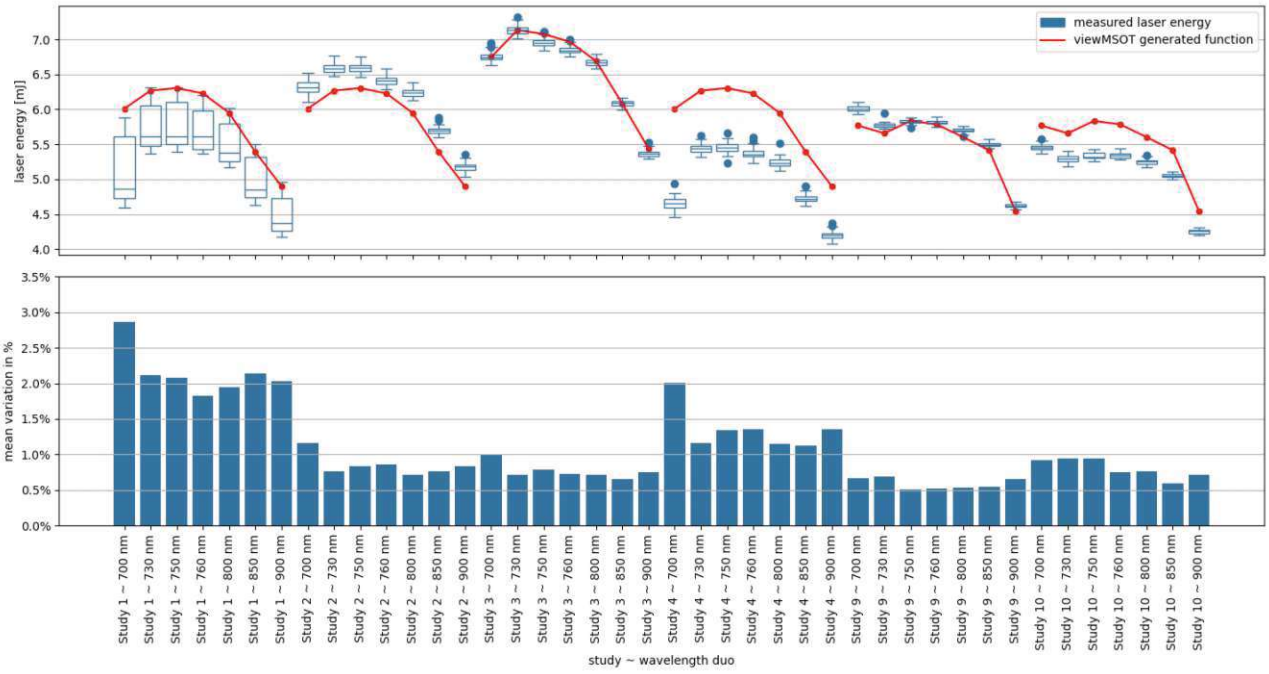


**Figure 19.** Stability of the laser pulse energies per study-wavelength duo throughout the study sessions; upper graph: the red lines represent the calibrated laser pulse energies by viewMSOT, while the box-plots represent the measured laser pulse energies; lower graph: percentage errors per study-wavelength duo

The calibrated laser pulse energies for Zerdine studies 1,2, and 4 followed the same pattern, with only Study 3 deviating. For the gel wax studies 9 and 10, the calibration functions were consistent but differs from the Zerdine studies, showing a bend at 730 $nm$. Both the calibrated and measured laser pulse energies for the gel wax studies showed a bend at 730 $nm$, unlike those observed in the Zerdine studies.

The significant variations in measured laser pulse energies during Study 1 can be attributed to a gradual decrease in laser energies at the start of the scanning session (Figure 20). In Study 2, the measured laser pulse energies were higher than the calibrated laser pulse energies. In Study 3, the measured and calibrated laser pulse energies aligned closely. In Study 4, the measured laser pulse energies were notably lower than the calibrated values. For Study 9, the measured laser pulse energies aligned with the calibrated values. In Study 10, the measured laser pulse energies were slightly below the calibrated levels.

Figure 20 provides a detailed view of the behaviour of the measured laser energies. The columns represent each study, while the rows correspond to specific illumination wavelengths. The x-axis ticks represent the sequence of recorded scan numbers and the y-axis shows the laser energies in $mJ$.

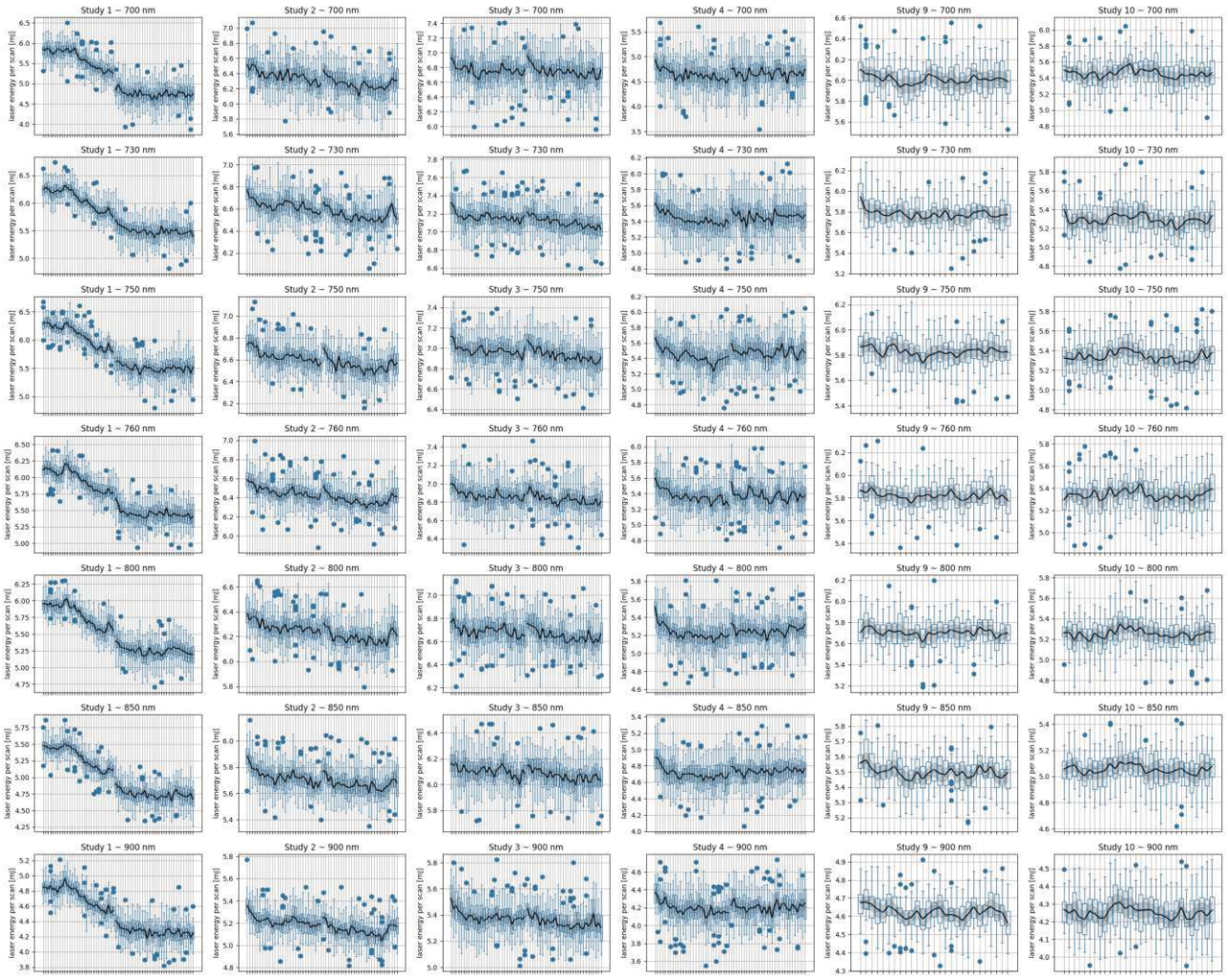


**Figure 20.** Detailed illustration of the behavior of the measured laser pulse energies

Table 8 provides a detailed overview of the average percentage errors within individual studies. Table 9 provides a detailed overview of the average percentage errors across the study sessions.

| study | I_nr | before | p [%] | p_I_nr [%] | p_study [%] | p_overall [%] |
|---|---|---|---|---|---|---|
| Study_1 | 1.0 | True | 2.77 | 2.04 | 2.14 | 1.23 |
| | | False | 1.3 | | | |
| | 2.0 | True | 3.26 | 2.28 | | |
| | | False | 1.31 | | | |
| | 3.0 | True | 3.28 | 2.11 | | |
| | | False | 0.94 | | | |
| Study_2 | 1.0 | True | 0.93 | 0.95 | 0.85 | |
| | | False | 0.98 | | | |
| | 2.0 | True | 0.9 | 0.83 | | |
| | | False | 0.77 | | | |
| | 3.0 | True | 0.74 | 0.76 | | |
| | | False | 0.77 | | | |
| Study_3 | 1.0 | True | 0.87 | 0.87 | 0.77 | |
| | | False | 0.87 | | | |
| | 2.0 | True | 0.71 | 0.76 | | |
| | | False | 0.8 | | | |
| | 3.0 | True | 0.62 | 0.68 | | |
| | | False | 0.74 | | | |
| Study_4 | 1.0 | True | 1.88 | 1.52 | 1.36 | |
| | | False | 1.16 | | | |
| | 2.0 | True | 1.56 | 1.36 | | |
| | | False | 1.15 | | | |
| | 3.0 | True | 1.38 | 1.19 | | |
| | | False | 1.0 | | | |
| Study_9 | - | - | - | - | 0.59 | |
| Study_10 | - | - | - | - | 0.8 | |

**Table 8.** Detailed percentage errors of the measured laser pulse energies; in-study variability

| I_nr | before | p [%] | p_I_nr [%] | p_overall [%] |
|---|---|---|---|---|
| 1 | True | 10.14 | 10.91 | 11.03 |
| | False | 11.67 | | |
| 2 | True | 10.38 | 11.05 | |
| | False | 11.72 | | |
| 3 | True | 10.57 | 11.14 | |
| | False | 11.71 | | |

**Table 9.** Detailed percentage errors of the measured laser pulse energies; variability across study sessions 1-4, 9 and 10

During this phase of the project, the Acuity's laser self-test frequently yielded negative results, necessitating repeated repairs by the technician. As the device was also used by other colleagues, inconsistencies in the calibration files occurred across studies. The evaluation of laser pulse energy revealed an in-study variation of 1.23% and an overall variation of 11.03%.

## 4.3 Frame Number Quantification

The frame number was defined in the preset and refers to the number of images generated per wavelength during a scan. These images were averaged to reduce noise, producing a single reconstructed image. During scanning, the progress of frame recording was displayed through an ascending bar (Figure 4). If there were no detector movement induced variations, the bar increases steadily. The motion sensitivity factor could be adjusted. Upon completing the scan, the corresponding series of images were saved in the relevant scan file (Figure 11).

The default frame number value was raised from 10 to 25 to assess its impact on image quality. Data acquisition and processing are discussed in detail in in 3.4 Data Processing and Data Analysis.

Figure 21 illustrates the variation of absorber and non-absorber signals within a study as a function of the frame number.

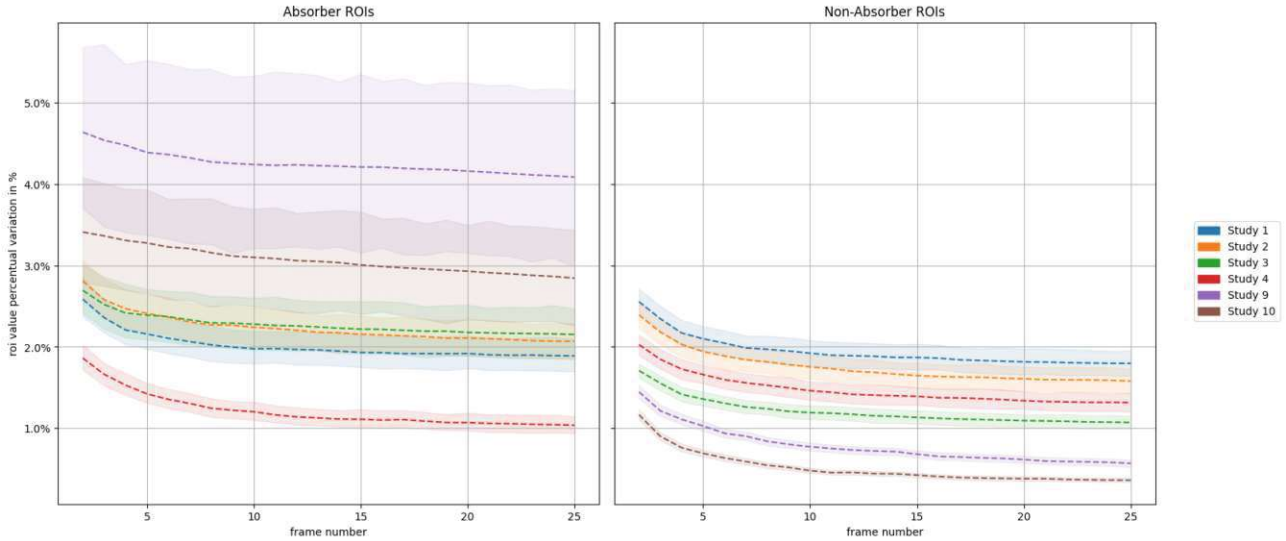


**Figure 21.** Variation of absorber (left) and non-absorber (right) signals within a study as a function of the frame number

Table 10 and Table 11 present the average signal value variation improvements categorized by study and ROI type (absorber/non-absorber).

| absorber | Study_1 | Study_2 | Study_3 | Study_4 | Study_9 | Study_10 |
|---|---|---|---|---|---|---|
| 2 | 2.59 | 2.81 | 2.69 | 1.86 | 4.64 | 3.41 |
| 10 | 1.98 | 2.24 | 2.28 | 1.2 | 4.24 | 3.1 |
| 25 | 1.89 | 2.07 | 2.15 | 1.03 | 4.09 | 2.84 |

**Table 10.** Average absorber signal value variation improvements categorized by study; in-study variability

| non-absorber | Study_1 | Study_2 | Study_3 | Study_4 | Study_9 | Study_10 |
|---|---|---|---|---|---|---|
| 2 | 2.55 | 2.39 | 1.71 | 2.03 | 1.45 | 1.16 |
| 10 | 1.92 | 1.75 | 1.19 | 1.46 | 0.77 | 0.48 |
| 25 | 1.8 | 1.58 | 1.07 | 1.31 | 0.57 | 0.36 |

**Table 11.** Average non-absorber signal value variation improvements categorized by study; in-study variability

Increasing the frame number from 2 to 10 frames yields an average improvement of 0.56%, while increasing from 10 to 25 frames results in an average improvement of 0.15%. Assessing the impact of frame number on image quality could be more thoroughly evaluated as a standalone project involving additional types of analysis, such as examining the signal-to-noise ratio. However, this would extend beyond the scope of the current project.

## 4.4 Optical Density Evaluation of Gel Wax Matrix and Absorbers

This chapter explores the variability in gel wax manufacturing by analysing the stability of optical density values measured using a photo-spectrometer. The absorption coefficient was determined for samples consisting exclusively of absorbing material. The preparation process for the different batches, as well as the sample preparation and the evaluation of the absorption coefficient, are detailed in 3.2.2 Gel Wax Phantom and 3.4 Data Processing and Data Analysis.

The composition of selected sGW and aGW stock solutions are presented in Table 12 and Table 13. The composition of the various absorbing batches used for the inclusions are provided in Table 14, Table 15 and Table 16.

| Name | cGW [g] | Ti$O_2$ [g] | Prepared on |
|---|---|---|---|
| sGW1 | 409 | 0.05 | 2018-08-13 |
| sGW2 | 409 | 0.05 | 2018-09-17 |
| sGW3 | 409 | 0.05 | 2018-11-30 |
| sGW4 | 409 | 0.05 | 2019-01-27 |

**Table 12.** Composition of sGW batches used as matrix and coating materials, as well as for inclusion preparation

| Name | cGW [g] | Ink [g] | Prepared on |
|---|---|---|---|
| aGW1 | 327 | 4 | 2018-11-30 |
| aGW2 | 409 | 5 | 2019-01-11 |

**Table 13.** Composition of aGW batches used for the preparation of inclusions

| absorber # | 1 | 2 | 3 | 4 | 5 | 6 | 7 |
|---|---|---|---|---|---|---|---|
| aGW1 [g] | 1 | 5 | 10 | 15 | 20 | 25 | 30 |
| cGW [g] | 49 | 45 | 40 | 35 | 30 | 25 | 20 |

**Table 14.** Composition of the aGWia used in Study 9

| absorber # | 1 | 2 | 3 | 4 | 5 | 6 | 7 | 8 | 9 | 10 |
|---|---|---|---|---|---|---|---|---|---|---|
| aGW2 [g] | 0.25 | 0.5 | 1 | 1.5 | 2 | 2.5 | 3 | 3.5 | 4 | 4.5 |
| cGW [g] | 49.75 | 49.5 | 49 | 48.5 | 48 | 47.5 | 47 | 46.5 | 46 | 45.5 |

**Table 15.** Composition of the aGWia, for which no MSOT Acuity study exists

| absorber # | 1 | 2 | 3 | 4 | 5 | 6 | 7 | 8 | 9 | 10 |
|---|---|---|---|---|---|---|---|---|---|---|
| aGW2 [g] | 0.25 | 0.5 | 1 | 1.5 | 2 | 2.5 | 3 | 3.5 | 4 | 4.5 |
| sGW4 [g] | 49.75 | 49.5 | 49 | 48.5 | 48 | 47.5 | 47 | 46.5 | 46 | 45.5 |

**Table 16.** Composition of the asGWia, for which no MSOT Acuity study exists

Figure 22 displays the absorbance values measured from the sample materials. The graph on the left illustrates the optical density values for the sGW batches listed in Table 12. A sample from the sGW4 batch was identified as an outlier and subsequently excluded from further analysis. The corresponding data points are indicated with red crosses in the graph for clarity. The middle graph presents the optical density values of the various aGWia batches listed in Table 13. The graph on the right provides a comparison of various aGWia and asGWia batches prepared in January 2019 listed in Table 15 and Table 16.

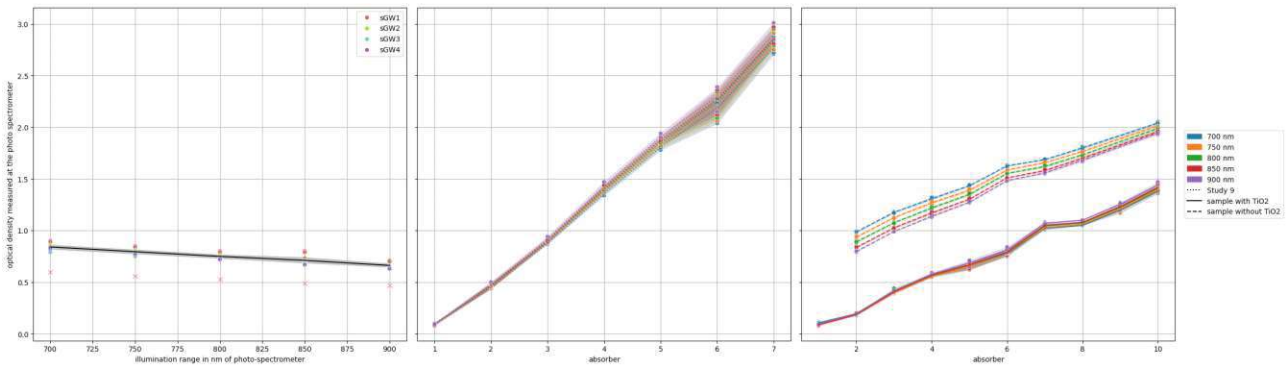


**Figure 22.** Optical density values measured from the sample materials; left: sGW sample material; middle: aGWia sample material (Study 9); right: comparison of aGWia and asGWia sample materials prepared in January 2019

Table 17, Table 18, Table 19 and Table 20 provide the measured optical density values from the photo-spectrometer and percentage errors for different types, categorized by batch number and wavelength. Table 18 and Table 19 also include the calculated $\mu_a$ values.

| wlg | batch | OD | p [%] (*) | p_wlg [%] (**) | p_overall [%] (***) |
|---|---|---|---|---|---|
| 700 nm | sGW1 | 0.88 ± 0.02 | 2.27 | 4.76 | 4.83 |
| | sGW2 | 0.85 ± 0.01 | 1.18 | | |
| | sGW3 | 0.8 ± 0.01 | 1.25 | | |
| | sGW4 | 0.82 ± 0.01 | 1.22 | | |
| 750 nm | sGW1 | 0.84 ± 0.02 | 2.38 | 3.8 | |
| | sGW2 | 0.8 ± 0.01 | 1.25 | | |
| | sGW3 | 0.76 ± 0.01 | 1.32 | | |
| | sGW4 | 0.77 ± 0.0 | 0.0 | | |
| 800 nm | sGW1 | 0.79 ± 0.01 | 1.27 | 4.0 | |
| | sGW2 | 0.75 ± 0.01 | 1.33 | | |
| | sGW3 | 0.72 ± 0.01 | 1.39 | | |
| | sGW4 | 0.72 ± 0.0 | 0.0 | | |
| 850 nm | sGW1 | 0.77 ± 0.04 | 5.19 | 7.04 | |
| | sGW2 | 0.7 ± 0.01 | 1.43 | | |
| | sGW3 | 0.68 ± 0.01 | 1.47 | | |
| | sGW4 | 0.67 ± 0.0 | 0.0 | | |
| 900 nm | sGW1 | 0.7 ± 0.01 | 1.43 | 4.55 | |
| | sGW2 | 0.66 ± 0.0 | 0.0 | | |
| | sGW3 | 0.64 ± 0.01 | 1.56 | | |
| | sGW4 | 0.63 ± 0.0 | 0.0 | | |

**Table 17.** Measured optical density values of various sGW batches and percentage errors for different types, categorized by batch number and wavelength; (*) in-sample variation, (**) in-wavelength across batch variation, (***) variation across wavelength-batch

| abs # | wlg | OD | $\mu_a$ | p [%] | p_a_val [%] | p_overall [%] |
|---|---|---|---|---|---|---|
| 1 | 700 nm | 0.1 ± 0.0 | 0.23 ± 0.0 | 0.0 | 8.89 | 4.16 |
| | 750 nm | 0.09 ± 0.01 | 0.22 ± 0.01 | 11.11 | | |
| | 800 nm | 0.09 ± 0.01 | 0.22 ± 0.01 | 11.11 | | |
| | 850 nm | 0.09 ± 0.01 | 0.2 ± 0.02 | 11.11 | | |
| | 900 nm | 0.09 ± 0.01 | 0.22 ± 0.01 | 11.11 | | |
| 2 | 700 nm | 0.46 ± 0.02 | 1.05 ± 0.05 | 4.35 | 5.62 | |
| | 750 nm | 0.46 ± 0.02 | 1.05 ± 0.05 | 4.35 | | |
| | 800 nm | 0.46 ± 0.03 | 1.07 ± 0.06 | 6.52 | | |
| | 850 nm | 0.46 ± 0.03 | 1.07 ± 0.06 | 6.52 | | |
| | 900 nm | 0.47 ± 0.03 | 1.09 ± 0.06 | 6.38 | | |
| 3 | 700 nm | 0.88 ± 0.01 | 2.02 ± 0.03 | 1.14 | 1.55 | |
| | 750 nm | 0.89 ± 0.01 | 2.04 ± 0.02 | 1.12 | | |
| | 800 nm | 0.9 ± 0.01 | 2.07 ± 0.03 | 1.11 | | |
| | 850 nm | 0.9 ± 0.02 | 2.07 ± 0.04 | 2.22 | | |
| | 900 nm | 0.92 ± 0.02 | 2.12 ± 0.04 | 2.17 | | |
| 4 | 700 nm | 1.36 ± 0.03 | 3.13 ± 0.06 | 2.21 | 2.15 | |
| | 750 nm | 1.38 ± 0.03 | 3.17 ± 0.07 | 2.17 | | |
| | 800 nm | 1.4 ± 0.03 | 3.22 ± 0.06 | 2.14 | | |
| | 850 nm | 1.41 ± 0.03 | 3.24 ± 0.07 | 2.13 | | |
| | 900 nm | 1.43 ± 0.03 | 3.3 ± 0.08 | 2.1 | | |
| 5 | 700 nm | 1.81 ± 0.03 | 4.16 ± 0.07 | 1.66 | 1.62 | |
| | 750 nm | 1.83 ± 0.03 | 4.21 ± 0.07 | 1.64 | | |
| | 800 nm | 1.86 ± 0.03 | 4.28 ± 0.07 | 1.61 | | |
| | 850 nm | 1.88 ± 0.03 | 4.32 ± 0.07 | 1.6 | | |
| | 900 nm | 1.91 ± 0.03 | 4.39 ± 0.07 | 1.57 | | |
| 6 | 700 nm | 2.19 ± 0.13 | 5.04 ± 0.3 | 5.94 | 5.8 | |
| | 750 nm | 2.21 ± 0.13 | 5.1 ± 0.31 | 5.88 | | |
| | 800 nm | 2.24 ± 0.13 | 5.17 ± 0.31 | 5.8 | | |
| | 850 nm | 2.27 ± 0.13 | 5.22 ± 0.3 | 5.73 | | |
| | 900 nm | 2.3 ± 0.13 | 5.3 ± 0.31 | 5.65 | | |
| 7 | 700 nm | 2.77 ± 0.09 | 6.37 ± 0.21 | 3.25 | 3.46 | |
| | 750 nm | 2.8 ± 0.1 | 6.45 ± 0.22 | 3.57 | | |
| | 800 nm | 2.84 ± 0.1 | 6.55 ± 0.22 | 3.52 | | |
| | 850 nm | 2.86 ± 0.1 | 6.59 ± 0.22 | 3.5 | | |
| | 900 nm | 2.9 ± 0.1 | 6.68 ± 0.22 | 3.45 | | |

**Table 18.** Measured optical density values of various aGWia (Study 9) batches with corresponding $\mu_a$ and percentage errors for different types, categorized by absorber and wavelength; in-absorber variation

| abs # | wlg | OD | $\mu_a$ | p [%] | p_a_val [%] | p_overall [%] |
|---|---|---|---|---|---|---|
| 1 | 700 nm | 0.11 ± 0.01 | 0.24 ± 0.01 | 9.09 | 10.04 | 3.33 |
| | 750 nm | 0.1 ± 0.01 | 0.22 ± 0.01 | 10.0 | | |
| | 800 nm | 0.1 ± 0.01 | 0.22 ± 0.01 | 10.0 | | |
| | 850 nm | 0.09 ± 0.01 | 0.2 ± 0.02 | 11.11 | | |
| | 900 nm | 0.1 ± 0.01 | 0.22 ± 0.01 | 10.0 | | |
| 2 | 700 nm | 0.19 ± 0.01 | 0.45 ± 0.01 | 5.26 | 5.21 | |
| | 750 nm | 0.19 ± 0.01 | 0.43 ± 0.02 | 5.26 | | |
| | 800 nm | 0.19 ± 0.01 | 0.43 ± 0.02 | 5.26 | | |
| | 850 nm | 0.19 ± 0.01 | 0.43 ± 0.02 | 5.26 | | |
| | 900 nm | 0.2 ± 0.01 | 0.45 ± 0.01 | 5.0 | | |
| 3 | 700 nm | 0.4 ± 0.01 | 0.92 ± 0.02 | 2.5 | 2.92 | |
| | 750 nm | 0.4 ± 0.01 | 0.92 ± 0.02 | 2.5 | | |
| | 800 nm | 0.42 ± 0.02 | 0.96 ± 0.05 | 4.76 | | |
| | 850 nm | 0.41 ± 0.01 | 0.93 ± 0.01 | 2.44 | | |
| | 900 nm | 0.42 ± 0.01 | 0.96 ± 0.02 | 2.38 | | |
| 4 | 700 nm | 0.56 ± 0.01 | 1.28 ± 0.02 | 1.79 | 1.76 | |
| | 750 nm | 0.56 ± 0.01 | 1.28 ± 0.02 | 1.79 | | |
| | 800 nm | 0.57 ± 0.01 | 1.31 ± 0.03 | 1.75 | | |
| | 850 nm | 0.57 ± 0.01 | 1.31 ± 0.03 | 1.75 | | |
| | 900 nm | 0.58 ± 0.01 | 1.33 ± 0.03 | 1.72 | | |
| 5 | 700 nm | 0.66 ± 0.03 | 1.51 ± 0.07 | 4.55 | 4.48 | |
| | 750 nm | 0.66 ± 0.03 | 1.51 ± 0.07 | 4.55 | | |
| | 800 nm | 0.67 ± 0.03 | 1.54 ± 0.08 | 4.48 | | |
| | 850 nm | 0.67 ± 0.03 | 1.54 ± 0.08 | 4.48 | | |
| | 900 nm | 0.69 ± 0.03 | 1.58 ± 0.07 | 4.35 | | |
| 6 | 700 nm | 0.78 ± 0.03 | 1.8 ± 0.07 | 3.85 | 3.79 | |
| | 750 nm | 0.79 ± 0.03 | 1.81 ± 0.07 | 3.8 | | |
| | 800 nm | 0.79 ± 0.03 | 1.82 ± 0.07 | 3.8 | | |
| | 850 nm | 0.79 ± 0.03 | 1.82 ± 0.07 | 3.8 | | |
| | 900 nm | 0.81 ± 0.03 | 1.87 ± 0.07 | 3.7 | | |
| 7 | 700 nm | 1.02 ± 0.01 | 2.35 ± 0.02 | 0.98 | 0.96 | |
| | 750 nm | 1.03 ± 0.01 | 2.36 ± 0.01 | 0.97 | | |
| | 800 nm | 1.04 ± 0.01 | 2.4 ± 0.03 | 0.96 | | |
| | 850 nm | 1.05 ± 0.01 | 2.42 ± 0.02 | 0.95 | | |
| | 900 nm | 1.07 ± 0.01 | 2.47 ± 0.03 | 0.93 | | |
| 8 | 700 nm | 1.05 ± 0.0 | 2.42 ± 0.0 | 0.0 | 0.19 | |
| | 750 nm | 1.06 ± 0.0 | 2.44 ± 0.0 | 0.0 | | |
| | 800 nm | 1.07 ± 0.01 | 2.48 ± 0.01 | 0.93 | | |
| | 850 nm | 1.08 ± 0.0 | 2.49 ± 0.0 | 0.0 | | |
| | 900 nm | 1.1 ± 0.0 | 2.53 ± 0.0 | 0.0 | | |
| 9 | 700 nm | 1.2 ± 0.02 | 2.76 ± 0.05 | 1.67 | 1.8 | |
| | 750 nm | 1.21 ± 0.02 | 2.78 ± 0.05 | 1.65 | | |
| | 800 nm | 1.22 ± 0.02 | 2.82 ± 0.05 | 1.64 | | |
| | 850 nm | 1.23 ± 0.03 | 2.83 ± 0.06 | 2.44 | | |
| | 900 nm | 1.25 ± 0.02 | 2.89 ± 0.05 | 1.6 | | |
| 10 | 700 nm | 1.38 ± 0.03 | 3.18 ± 0.06 | 2.17 | 2.13 | |
| | 750 nm | 1.39 ± 0.03 | 3.21 ± 0.06 | 2.16 | | |
| | 800 nm | 1.41 ± 0.03 | 3.25 ± 0.06 | 2.13 | | |
| | 850 nm | 1.42 ± 0.03 | 3.26 ± 0.07 | 2.11 | | |
| | 900 nm | 1.44 ± 0.03 | 3.32 ± 0.06 | 2.08 | | |

**Table 19.** Measured optical density values of various aGWia (January 2019) batches with corresponding $\mu_a$ and percentage errors for different types, categorized by absorber and wavelength; in-absorber variation

| abs # | wlg | OD | $\mu_a$ | p [%] | p_a_val [%] | p_overall [%]] |
|---|---|---|---|---|---|---|
| 1 | 700 nm | nan ± nan | - | - | - | 0.75 |
| | 750 nm | nan ± nan | - | - | | |
| | 800 nm | nan ± nan | - | - | | |
| | 850 nm | nan ± nan | - | - | | |
| | 900 nm | nan ± nan | - | - | | |
| 2 | 700 nm | 0.99 ± 0.01 | - | 1.01 | 1.13 | |
| | 750 nm | 0.94 ± 0.01 | - | 1.06 | | |
| | 800 nm | 0.89 ± 0.01 | - | 1.12 | | |
| | 850 nm | 0.84 ± 0.01 | - | 1.19 | | |
| | 900 nm | 0.8 ± 0.01 | - | 1.25 | | |
| 3 | 700 nm | 1.18 ± 0.01 | - | 0.85 | 0.73 | |
| | 750 nm | 1.13 ± 0.01 | - | 0.88 | | |
| | 800 nm | 1.08 ± 0.01 | - | 0.93 | | |
| | 850 nm | 1.03 ± 0.01 | - | 0.97 | | |
| | 900 nm | 0.99 ± 0.0 | - | 0.0 | | |
| 4 | 700 nm | 1.31 ± 0.01 | - | 0.76 | 0.82 | |
| | 750 nm | 1.27 ± 0.01 | - | 0.79 | | |
| | 800 nm | 1.22 ± 0.01 | - | 0.82 | | |
| | 850 nm | 1.17 ± 0.01 | - | 0.85 | | |
| | 900 nm | 1.14 ± 0.01 | - | 0.88 | | |
| 5 | 700 nm | 1.43 ± 0.01 | - | 0.7 | 0.74 | |
| | 750 nm | 1.39 ± 0.01 | - | 0.72 | | |
| | 800 nm | 1.35 ± 0.01 | - | 0.74 | | |
| | 850 nm | 1.3 ± 0.01 | - | 0.77 | | |
| | 900 nm | 1.27 ± 0.01 | - | 0.79 | | |
| 6 | 700 nm | 1.63 ± 0.01 | - | 0.61 | 0.51 | |
| | 750 nm | 1.59 ± 0.01 | - | 0.63 | | |
| | 800 nm | 1.55 ± 0.01 | - | 0.65 | | |
| | 850 nm | 1.51 ± 0.0 | - | 0.0 | | |
| | 900 nm | 1.48 ± 0.01 | - | 0.68 | | |
| 7 | 700 nm | 1.69 ± 0.01 | - | 0.59 | 0.62 | |
| | 750 nm | 1.66 ± 0.01 | - | 0.6 | | |
| | 800 nm | 1.62 ± 0.01 | - | 0.62 | | |
| | 850 nm | 1.58 ± 0.01 | - | 0.63 | | |
| | 900 nm | 1.56 ± 0.01 | - | 0.64 | | |
| 8 | 700 nm | 1.8 ± 0.01 | - | 0.56 | 0.58 | |
| | 750 nm | 1.77 ± 0.01 | - | 0.56 | | |
| | 800 nm | 1.73 ± 0.01 | - | 0.58 | | |
| | 850 nm | 1.7 ± 0.01 | - | 0.59 | | |
| | 900 nm | 1.68 ± 0.01 | - | 0.6 | | |
| 9 | 700 nm | nan ± nan | - | - | - | |
| | 750 nm | nan ± nan | - | - | | |
| | 800 nm | nan ± nan | - | - | | |
| | 850 nm | nan ± nan | - | - | | |
| | 900 nm | nan ± nan | - | - | | |
| 10 | 700 nm | 2.04 ± 0.01 | - | 0.49 | 0.91 | |
| | 750 nm | 2.01 ± 0.02 | - | 1.0 | | |
| | 800 nm | 1.99 ± 0.02 | - | 1.01 | | |
| | 850 nm | 1.96 ± 0.02 | - | 1.02 | | |
| | 900 nm | 1.94 ± 0.02 | - | 1.03 | | |

**Table 20.** Measured optical density values of various asGWia (January 2019) batches and percentage errors for different types, categorized by absorber and wavelength; in-absorber variation

In the 700 – 900 $nm$ range, the optical density values exhibit a linear decrease with increasing wavelength and increase proportionally with the concentration of the absorbing material. The analysis of gel wax sample variability demonstrated an across-batch variation in sGW of 4.83%, an in-absorber variation in aGW (Study 9) of 4.16%, an in-absorber variation in aGWia of 3.33% and an in-absorber variation in asGWia of 0.75%. It's worth mentioning that studies 9 and 10 were initially designed for testing purposes only, which limited the data quality. The original intent was to scan absorbers embedded in a phantom matrix material started to prepare in January 2019; however, due to time constrains, these studies could not be completed.

## 4.5 Absorber Signal Quantification

This chapter examines the variability of absorber signals in the Zerdine phantom, analysing both within-study fluctuations and variations across multiple study sessions, as well as the within-study variability of the gel wax absorbers. 3.4 Data Processing and Data Analysis outlines the process of extracting the absorber ROIs from the images for quantification and details about the subsequent processing and analysis of this data.

Figure 23 and Figure 24 present the results of the absorber signal values from studies 1-4, 9 and 10. The top section displays the signal values for each absorber-position-wavelength trio / absorber-wavelength duo in a box-plot. The bottom section features bar-plots illustrating the percentage errors of the corresponding trios/duos.

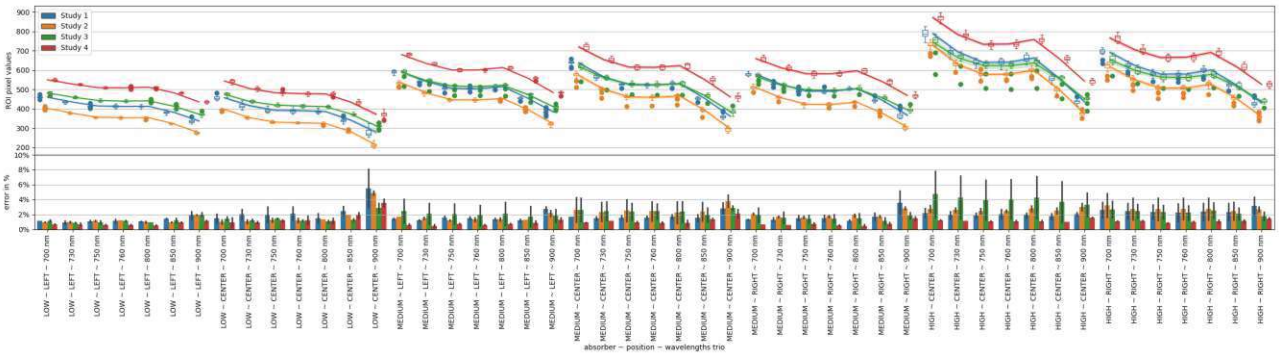


**Figure 23.** Absorber signal values from studies 1-4 per absorber-position-wavelength trio and corresponding percentage errors

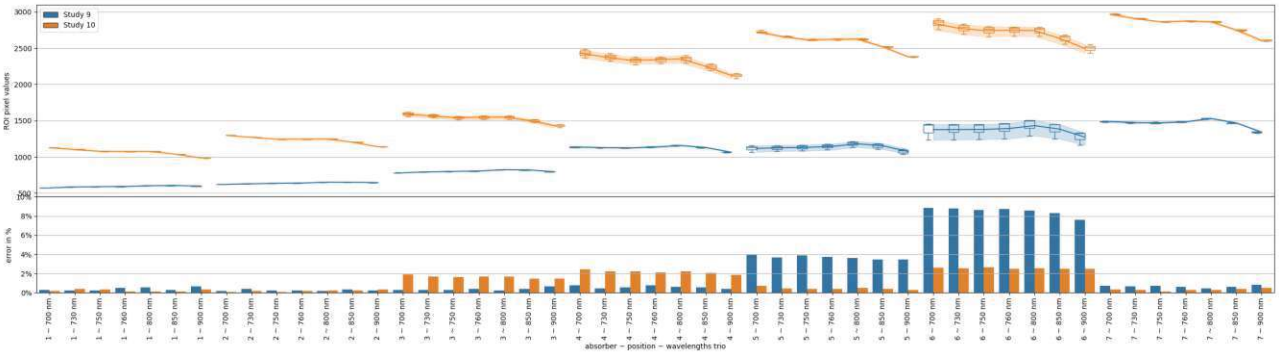


**Figure 24.** Absorber signal values from studies 9 and 10 per absorber-wavelength duo and corresponding percentage errors

As expected, the y-values rose proportionally with the increase of the absorber coefficient. The percentage errors also grew with higher absorber level. A wavelength-specific pattern was observed across all studies. Additionally, the absolute slope gradient between different wavelengths increased proportionally with the increasing absorption coefficient. The absorbers with $TiO_2$ coating (Study 10) showed higher signal values than those without coating (Study 9).

Table 21 and Table 23 provide a detailed overview of the average percentage errors within individual studies. Table 21 provides a detailed overview of the average percentage errors across the study sessions 1-4.

| study | boxplot_type | before | p [%] | p_boxplot_tyoe [%] | p_study [%] | p_overall [%] |
|---|---|---|---|---|---|---|
| Study_1 | LOW LEFT | True | 1.41 | 1.24 | 1.89 | 1.79 |
| | | after | 1.08 | | | |
| | LOW CENTER | True | 3.43 | 2.44 | | |
| | | False | 1.45 | | | |
| | MEDIUM LEFT | True | 1.71 | 1.57 | | |
| | | False | 1.44 | | | |
| | MEDIUM CENTER | True | 2.06 | 1.77 | | |
| | | False | 1.48 | | | |
| | MEDIUM RIGHT | True | 2.18 | 1.72 | | |
| | | False | 1.27 | | | |
| | HIGH CENTER | True | 2.37 | 1.95 | | |
| | | False | 1.54 | | | |
| | HIGH RIGHT | True | 3.6 | 2.51 | | |
| | | False | 1.42 | | | |
| Study_2 | LOW LEFT | True | 1.13 | 1.17 | 2.07 | |
| | | False | 1.21 | | | |
| | LOW CENTER | True | 1.64 | 1.82 | | |
| | | False | 2.0 | | | |
| | MEDIUM LEFT | True | 1.47 | 1.5 | | |
| | | False | 1.53 | | | |
| | MEDIUM CENTER | True | 1.33 | 2.63 | | |
| | | False | 3.93 | | | |
| | MEDIUM RIGHT | True | 1.89 | 1.94 | | |
| | | False | 1.99 | | | |
| | HIGH CENTER | True | 3.0 | 2.65 | | |
| | | False | 2.31 | | | |
| | HIGH RIGHT | True | 1.49 | 2.76 | | |
| | | False | 4.03 | | | |
| Study_3 | LOW LEFT | True | 1.09 | 1.18 | 2.15 | |
| | | False | 1.27 | | | |
| | LOW CENTER | True | 1.4 | 1.5 | | |
| | | False | 1.6 | | | |
| | MEDIUM LEFT | True | 3.37 | 2.03 | | |
| | | False | 0.68 | | | |
| | MEDIUM CENTER | True | 3.44 | 2.45 | | |
| | | False | 1.46 | | | |
| | MEDIUM RIGHT | True | 2.03 | 1.55 | | |
| | | False | 1.08 | | | |
| | HIGH CENTER | True | 6.65 | 4.04 | | |
| | | False | 1.42 | | | |
| | HIGH RIGHT | True | 3.2 | 2.31 | | |
| | | False | 1.42 | | | |
| Study_4 | LOW LEFT | True | 0.67 | 0.73 | 1.03 | |
| | | False | 0.79 | | | |
| | LOW CENTER | True | 1.19 | 1.56 | | |
| | | False | 1.92 | | | |
| | MEDIUM LEFT | True | 0.87 | 0.77 | | |
| | | False | 0.67 | | | |
| | MEDIUM CENTER | True | 0.97 | 1.17 | | |
| | | False | 1.37 | | | |
| | MEDIUM RIGHT | True | 0.69 | 0.75 | | |
| | | False | 0.8 | | | |
| | HIGH CENTER | True | 1.21 | 1.17 | | |
| | | False | 1.13 | | | |
| | HIGH RIGHT | True | 1.09 | 1.1 | | |
| | | False | 1.12 | | | |

**Table 21.** Absorber signal percentage errors from studies 1-4 in detail; in-study variability

| boxplot_type | before | p [%] | p_boxplot_type [%] | p_overall [%] |
|---|---|---|---|---|
| LOW LEFT | True | 13.55 | 13.43 | 11.87 |
| | False | 13.31 | | |
| LOW CENTER | True | 14.99 | 14.57 | |
| | False | 14.15 | | |
| MEDIUM LEFT | True | 11.62 | 11.28 | |
| | False | 10.93 | | |
| MEDIUM CENTER | True | 11.91 | 11.34 | |
| | False | 10.76 | | |
| MEDIUM RIGHT | True | 12.72 | 11.97 | |
| | False | 11.22 | | |
| HIGH CENTER | True | 10.88 | 9.83 | |
| | False | 8.78 | | |
| HIGH RIGHT | True | 11.41 | 10.68 | |
| | False | 9.94 | | |

**Table 22.** Absorber signal percentage errors from studies 1-4 in detail; variability across study sessions 1-4

| study | a_val | p_a_val [%] | p_study [%] | p_overall [%] |
|---|---|---|---|---|
| Study_9 | 1 | 0.41 | 2.07 | 1.58 |
| | 2 | 0.27 | | |
| | 3 | 0.37 | | |
| | 4 | 0.59 | | |
| | 5 | 3.68 | | |
| | 6 | 8.49 | | |
| | 7 | 0.66 | | |
| Study_10 | 1 | 0.24 | 1.08 | |
| | 2 | 0.2 | | |
| | 3 | 1.65 | | |
| | 4 | 2.17 | | |
| | 5 | 0.46 | | |
| | 6 | 2.56 | | |
| | 7 | 0.32 | | |

**Table 23.** Absorber signal percentage errors from studies 9 and 10 in detail; in-study variability

The analysis of absorber signals demonstrated an in-study variation of 1.79% and an overall variation of 11.87% across study sessions 1 to 4. Additionally, the in-study variation for study sessions 9 and 10 was found to be 1.58%.

## 4.6 Non-absorber Signal Quantification

This chapter examines the variability of non-absorber signals in the Zerdine phantom, analysing both within-study fluctuations and variations across multiple study sessions, as well as the within-study variability of the gel wax non-absorber signals. 3.4 Data Processing and

Data Analysis outlines the process of extracting the non-absorber ROIs from the images for quantification, and details about the subsequent processing and analysis of this data.

Figure 25 and Figure 26 display the non-absorber signal values from studies 1-4, 9 and 10. The top section of Figure 25 presents signal values for each trio consisting of 'name of the ROI' (Figure 18), 'absorber in the center of the FOV' (1 $\hat{=}$ high, 2 $\hat{=}$ medium, 3 $\hat{=}$ low) and wavelength whereas the top section of Figure 26 the signal values for each 'name of the ROI'-wavelength duo presents, represented as box-plots. The lower section illustrates the percentage errors of these trios/duos in a bar-plot format.

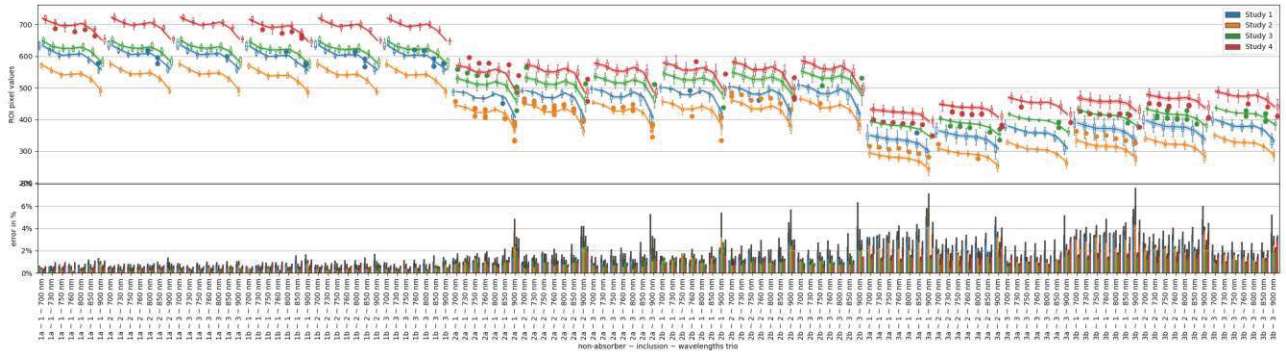


**Figure 25.** Non-Absorber signal values from studies 1-4 per 'name of the ROI'-'absorber in the center of the FOV'-wavelength trio and corresponding percentage errors

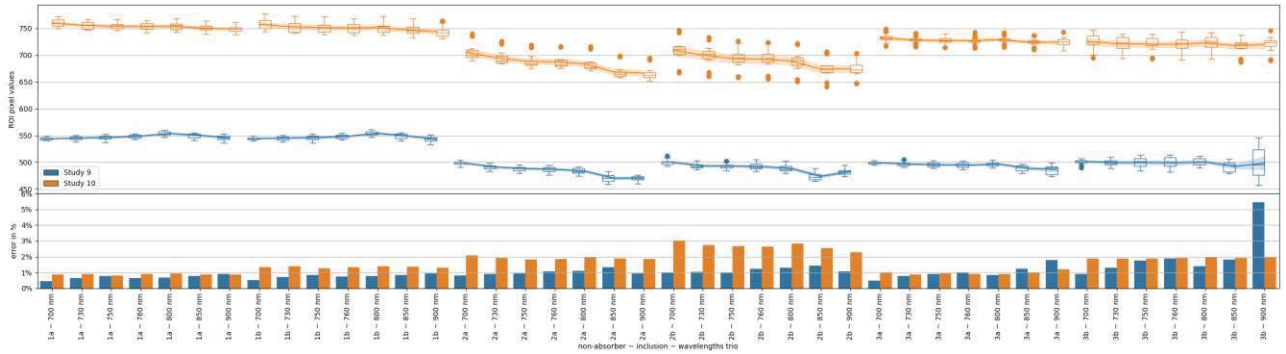


**Figure 26.** Non-Absorber signal values from studies 9 and 10 per 'name of the ROI'-wavelength duo and corresponding percentage errors

Figure 25 shows that the y-values in the upper image areas (1a, 1b) exhibited greater absorption compared to the lower areas (2a, 2b, 3a, 3b). In the lower regions, the influence of the absorber positioned at the center of the field of view became more pronounced, while in the upper regions, this central absorber appeared to have minimal impact.

In Figure 26, the absorber dependency was not specifically highlighted; however, detailed plot (not shown here) indicate that the absorbance-dependent effect was absent in this dataset. Nonetheless, signal value variations increased with greater image depth, though this effect remains minimal. Interestingly, the middle ROI position exhibited the lowest signal values.

However, examining the impact of ROI positioning across the entire image is beyond the scope of this thesis.

Table 24 and Table 26 provide a detailed overview of the average percentage errors within individual studies. Table 25 provides a detailed overview of the average percentage errors across the study sessions 1-4.

| study | non_absorber | before | p [%] | p_non_absorber [%] | p_study [%] | p_overall [%] |
|---|---|---|---|---|---|---|
| Study_1 | 1a | True | 0.88 | 0.71 | 1.8 | 1.44 |
| | | False | 0.54 | | | |
| | 1b | True | 1.11 | 0.83 | | |
| | | False | 0.55 | | | |
| | 2a | True | 1.88 | 1.52 | | |
| | | False | 1.15 | | | |
| | 2b | True | 2.22 | 1.8 | | |
| | | False | 1.38 | | | |
| | 3a | True | 3.47 | 2.84 | | |
| | | False | 2.21 | | | |
| | 3b | True | 3.64 | 3.07 | | |
| | | False | 2.5 | | | |
| Study_2 | 1a | True | 0.67 | 0.55 | 1.58 | |
| | | False | 0.43 | | | |
| | 1b | True | 0.76 | 0.61 | | |
| | | False | 0.46 | | | |
| | 2a | True | 1.23 | 1.43 | | |
| | | False | 1.64 | | | |
| | 2b | True | 1.52 | 1.84 | | |
| | | False | 2.15 | | | |
| | 3a | True | 2.44 | 2.28 | | |
| | | False | 2.12 | | | |
| | 3b | True | 2.92 | 2.76 | | |
| | | False | 2.61 | | | |
| Study_3 | 1a | True | 0.48 | 0.39 | 1.07 | |
| | | False | 0.31 | | | |
| | 1b | True | 0.49 | 0.41 | | |
| | | False | 0.33 | | | |
| | 2a | True | 1.73 | 1.4 | | |
| | | False | 1.06 | | | |
| | 2b | True | 1.51 | 1.47 | | |
| | | False | 1.42 | | | |
| | 3a | True | 1.06 | 1.25 | | |
| | | False | 1.44 | | | |
| | 3b | True | 1.36 | 1.5 | | |
| | | False | 1.65 | | | |
| Study_4 | 1a | True | 0.47 | 0.6 | 1.31 | |
| | | False | 0.72 | | | |
| | 1b | True | 0.46 | 0.61 | | |
| | | False | 0.77 | | | |
| | 2a | True | 1.21 | 1.04 | | |
| | | False | 0.87 | | | |
| | 2b | True | 1.14 | 1.16 | | |
| | | False | 1.17 | | | |
| | 3a | True | 1.57 | 2.08 | | |
| | | False | 2.59 | | | |
| | 3b | True | 1.85 | 2.4 | | |
| | | False | 2.96 | | | |

**Table 24.** Non-absorber signal percentage errors from studies 1-4 in detail; in-study variability

| ROI name | before | p [%] | p_non_absorber [%] | p_overall [%] |
|---|---|---|---|---|
| 1a | True | 9.14 | 9.15 | 11.19 |
| | False | 9.16 | | |
| 1b | True | 9.11 | 9.14 | |
| | False | 9.17 | | |
| 2a | True | 10.99 | 9.92 | |
| | False | 8.85 | | |
| 2b | True | 10.81 | 9.61 | |
| | False | 8.42 | | |
| 3a | True | 15.24 | 15.25 | |
| | False | 15.26 | | |
| 3b | True | 13.89 | 14.06 | |
| | False | 14.23 | | |

**Table 25.** Non-absorber signal percentage errors from studies 1-4 in detail; variability across study sessions 1-4

| study | non_absorber | p [%] | p_study [%] | p_overall [%] |
|---|---|---|---|---|
| Study_9 | 1a | 0.69 | 1.11 | 1.36 |
| | 1b | 0.76 | | |
| | 2a | 1.02 | | |
| | 2b | 1.14 | | |
| | 3a | 1.0 | | |
| | 3b | 2.07 | | |
| Study_10 | 1a | 0.88 | 1.61 | |
| | 1b | 1.34 | | |
| | 2a | 1.91 | | |
| | 2b | 2.67 | | |
| | 3a | 0.96 | | |
| | 3b | 1.92 | | |

**Table 26.** Non-absorber signal percentage errors from studies 9 and 10 in detail; in-study variability

The analysis of non-absorber signals demonstrated an in-study variation of 1.44% and an overall variation of 11.19% across study sessions 1 to 4. Additionally, the in-study variation for study sessions 9 and 10 was found to be 1.36%.

## 4.7 Detector Sensitivity Field Quantification

This chapter evaluates the variability in system performance by analysing the sensitivity field of the detector. Data acquisition and processing are described in 3.4 Data Processing and Data Analysis.

Figure 27 shows the percentage difference between identical Zerdine absorbers placed at various positions and their corresponding percentage errors. The x-axis labels consist of the minuend,

subtrahend and the respective illumination wavelength. Positive values are displayed in the yellow area, while negative values appear in the blue area.

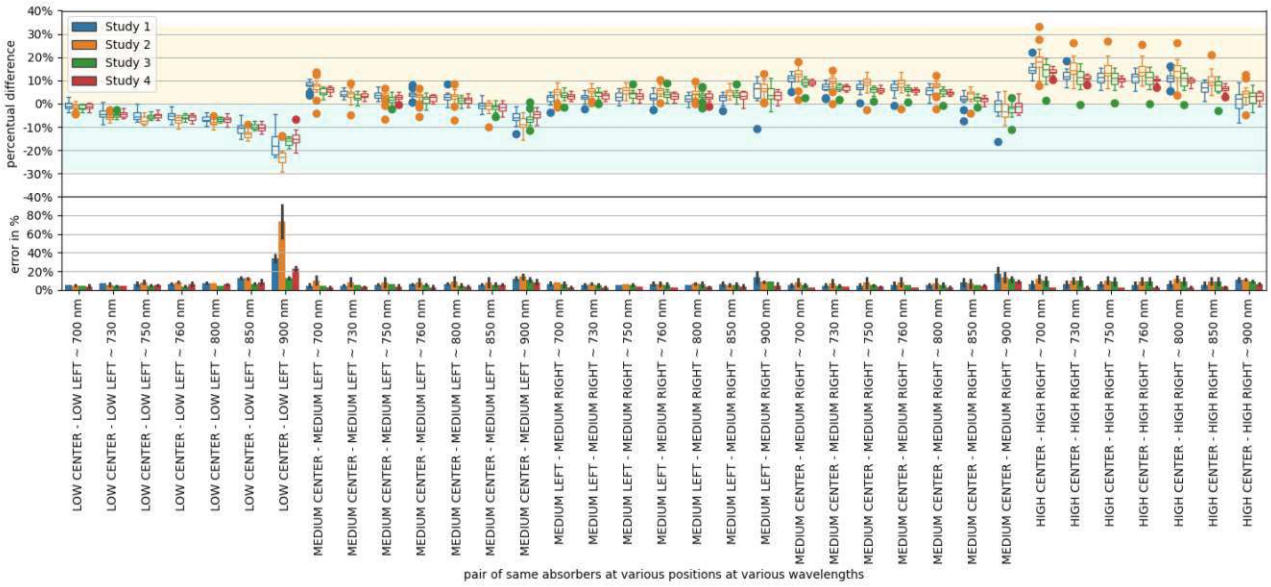


**Figure 27.** Percentage difference between identical Zerdine absorbers placed at various positions and their corresponding percentage errors

Sensitivity is expected to be highest at the center of the detector and this was anticipated to be reflected in the results. However, the findings, as presented in Figure 23, Figure 27 and Table 27, reveal unexpected outcomes. For the `low` absorber, the signal from the left edge is significantly higher than at the center, resulting in a negative difference between these values. The `medium` absorber results further highlight an unequal signal difference between the left and right edges of the image. Only the `high` absorber results meet expectations, with higher signal values observed at the center of the detector compared to the edges.

Table 27 details the average percentage differences and errors.

| **Pairs of same absorbers of difference evaluation** | **Mean percentage difference** [%] | **Mean percentage error** [%] |
|---|---|---|
| LOW CENTER - LOW LEFT | -7.61 | 10.51 |
| MEDIUM CENTER - MEDIUM LEFT | 1.44 | 6.52 |
| MEDIUM LEFT - MEDIUM RIGHT | 3.86 | 5.72 |
| MEDIUM CENTER - MEDIUM RIGHT | 5.32 | 6.37 |
| HIGH CENTER - HIGH RIGHT | 10.31 | 7.43 |

**Table 27.** Average percentage differences and percentage errors of the detector's sensitivity field

A reconstruction artefact is suspected to contribute to the unexpected results, indicating that the evaluation of the sensitivity field may be more effectively conducted using absorbers with

uniform absorption coefficients rather than the varying coefficients present in the Zerdine phantom. The analyses from both 4.5 Absorber Signal Quantification and 4.6 Non-absorber Signal Quantification revealed that the selection of the absorber positioned at the center of the detector had a significant impact on the overall image.

## 4.8 Offset Quantification

As outlined in the previous chapter, the overall image values were observed to vary based on the absorber positioned at the center of the field of view. This chapter investigates the impact of the central absorber on the minimum and maximum values of the image arrays. Definition, data acquisition and processing are described in 3.4 Data Processing and Data Analysis.

Figure 28 illustrates the minimum and maximum values of the image array for studies 1 through 4 as a function of wavelength. The dotted lines indicate data sets where the `high` absorber is positioned at the center of the field of view. The dashed lines represent data sets with the `medium` absorber at the center of the field of view. The solid lines corresponds to the data sets featuring the `low` absorber at the center of the field of view.

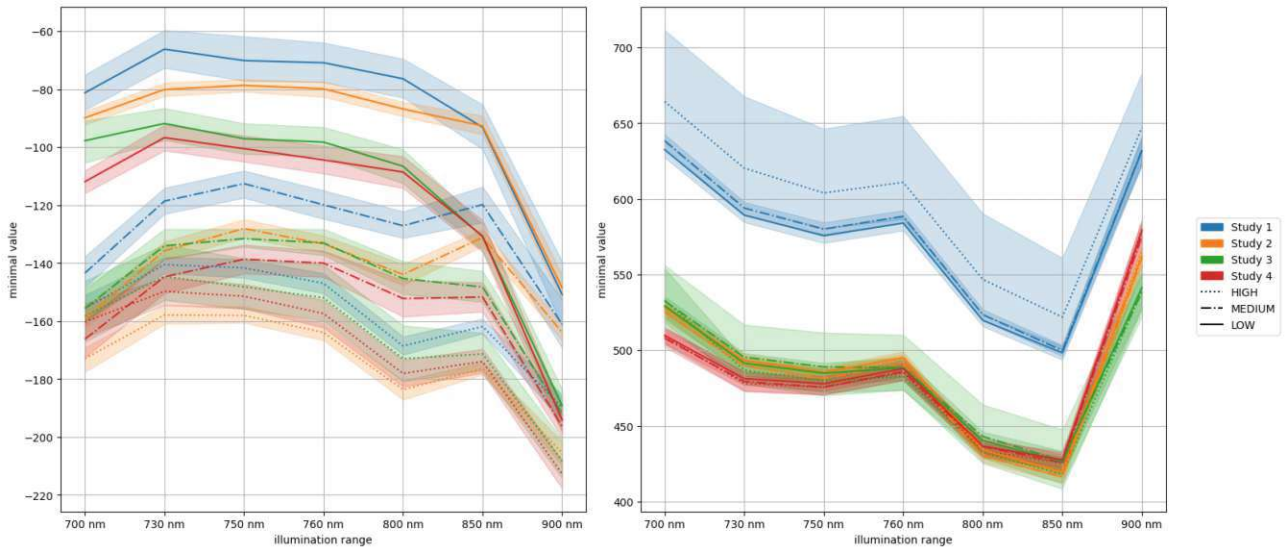


**Figure 28.** Minimum (left) and maximum (right) values of the image array for studies 1 through 4 as a function of wavelength; various line styles represent various absorbers positioned at the center of the field of view

Figure 29 displays absorbers of varying strengths for studies 9 and 10, with numbering explained in Table 14 of 4.4 Optical Density Evaluation of Gel Wax Matrix and Absorbers. The solid lines represent Study 9, while the dotted lines correspond to Study 10.

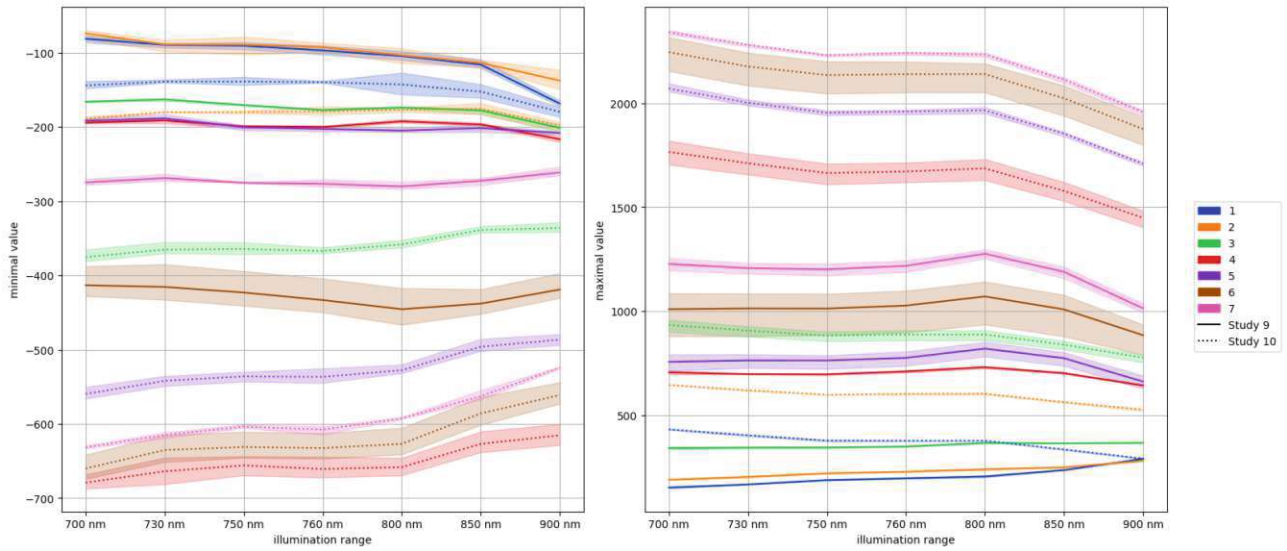


**Figure 29.** Minimum (left) and maximum (right) values of the image array for studies 9 (solid lines) and 10 (dotted lines) as a function of wavelength; various colors represent various absorbers

Figure 28 and Figure 29 illustrate the inverse relationship between minimum and maximum values. In the Zerdine studies, however, only the transition between 700 *nm* and 800 *nm* showed a direct proportional relationship.

For Zerdine, the variations in offset values was lower for images with the `high` absorber at the center of the field compared to those with the `low` absorber in the same position (Table 28). Conversely, the gel wax studies displayed an opposite trend, where offset value variations decreased with higher absorption concentrations (Table 30).

In both Zerdine and gel wax studies, the offset values exhibited greater variability than the maximum values (Table 28/Table 29, Table 30/Table 31).

Detailed percentage errors of the minimal and maximal pixel values for studies 1 through 4 are provided in Table 28 and Table 29. Detailed percentage errors of the minimal and maximal pixel values for studies 9 an 10 are provided in Table 30 and Table 31.

| study | I_nr | before | p [%] | p_I_nr [%] | p_study [%] | p_overall [%] |
|---|---|---|---|---|---|---|
| Study_1 | 1 | True | 6.28 | 5.0 | 7.78 | 6.84 |
| | | False | 3.73 | | | |
| | 2 | True | 7.66 | 6.75 | | |
| | | False | 5.85 | | | |
| | 3 | True | 15.79 | 11.58 | | |
| | | False | 7.36 | | | |
| Study_2 | 1 | True | 4.01 | 4.36 | 4.99 | |
| | | False | 4.71 | | | |
| | 2 | True | 4.42 | 4.63 | | |
| | | False | 4.84 | | | |
| | 3 | True | 6.31 | 5.97 | | |
| | | False | 5.63 | | | |
| Study_3 | 1 | True | 14.92 | 9.15 | 8.11 | |
| | | False | 3.38 | | | |
| | 2 | True | 8.27 | 6.78 | | |
| | | False | 5.28 | | | |
| | 3 | True | 8.43 | 8.4 | | |
| | | False | 8.37 | | | |
| Study_4 | 1 | True | 4.73 | 4.58 | 6.47 | |
| | | False | 4.43 | | | |
| | 2 | True | 6.68 | 6.9 | | |
| | | False | 7.11 | | | |
| | 3 | True | 8.32 | 7.92 | | |
| | | False | 7.52 | | | |

**Table 28.** Detailed percentage error of the minimal pixel values for studies 1 through 4; in-study variability

| study | I_nr | before | p [%] | p_I_nr [%] | p_study [%] | p_overall [%] |
|---|---|---|---|---|---|---|
| Study_1 | 1 | True | 2.23 | 11.59 | 4.91 | 3.26 |
| | | False | 20.96 | | | |
| | 2 | True | 1.89 | 1.55 | | |
| | | False | 1.21 | | | |
| | 3 | True | 2.02 | 1.58 | | |
| | | False | 1.15 | | | |
| Study_2 | 1 | True | 1.94 | 1.41 | 1.66 | |
| | | False | 0.89 | | | |
| | 2 | True | 1.45 | 2.17 | | |
| | | False | 2.89 | | | |
| | 3 | True | 1.72 | 1.39 | | |
| | | False | 1.06 | | | |
| Study_3 | 1 | True | 5.32 | 3.37 | 4.35 | |
| | | False | 1.41 | | | |
| | 2 | True | 3.7 | 7.21 | | |
| | | False | 10.72 | | | |
| | 3 | True | 3.55 | 2.49 | | |
| | | False | 1.42 | | | |
| Study_4 | 1 | True | 1.95 | 2.09 | 2.11 | |
| | | False | 2.22 | | | |
| | 2 | True | 2.03 | 2.0 | | |
| | | False | 1.98 | | | |
| | 3 | True | 2.5 | 2.24 | | |
| | | False | 1.97 | | | |

**Table 29.** Detailed percentage error of the maximal pixel values for studies 1 through 4; in-study variability

| study | a_val | p [%] | p_study [%] | p_overall [%] |
|---|---|---|---|---|
| Study_9 | 1 | 4.93 | 3.65 | 2.94 |
| | 2 | 9.05 | | |
| | 3 | 1.33 | | |
| | 4 | 1.21 | | |
| | 5 | 1.88 | | |
| | 6 | 5.41 | | |
| | 7 | 1.71 | | |
| Study_10 | 1 | 4.46 | 2.23 | |
| | 2 | 2.11 | | |
| | 3 | 1.85 | | |
| | 4 | 2.11 | | |
| | 5 | 1.6 | | |
| | 6 | 2.89 | | |
| | 7 | 0.58 | | |

**Table 30.** Detailed percentage error of the minimal pixel values for studies 9 and 10; in-study variability

| study | a_val | p [%] | p_study [%] | p_overall [%] |
|---|---|---|---|---|
| Study_9 | 1 | 1.44 | 3.11 | 2.4 |
| | 2 | 0.97 | | |
| | 3 | 1.03 | | |
| | 4 | 0.62 | | |
| | 5 | 4.63 | | |
| | 6 | 10.85 | | |
| | 7 | 2.25 | | |
| Study_10 | 1 | 0.78 | 1.69 | |
| | 2 | 0.43 | | |
| | 3 | 2.8 | | |
| | 4 | 2.99 | | |
| | 5 | 0.69 | | |
| | 6 | 3.71 | | |
| | 7 | 0.44 | | |

**Table 31.** Detailed percentage error of the maximal pixel values for studies 9 and 10; in-study variability

It was observed that as the maximum value in the image increased, the minimum value also rose. This artefact appeared due to image reconstruction process. The analysis of the minimum and maximum pixel values revealed an in-study variation of 6.84% and 3.26%, respectively, for studies 1 to 4. For study sessions 9 and 10, the in-study variation was determined to be 2.94% and 2.40%, respectively.

## 4.9 ROI Positioning Accuracy

This chapter explores the variability in the reproducibility of the acquisition process by evaluating the stability of ROI positioning both within individual studies and across multiple study sessions. Data acquisition and processing are described in 3.4 Data Processing and Data Analysis.

Figure 30 illustrates the variation in automated ROI positioning for the Zerdine studies. The graph on the left presents the variation in the x- and y-directions as box-plots, with the square figure representing the actual 233x233-pixel image array. The graph on the right displays the percentage variation in the x- and y-directions.

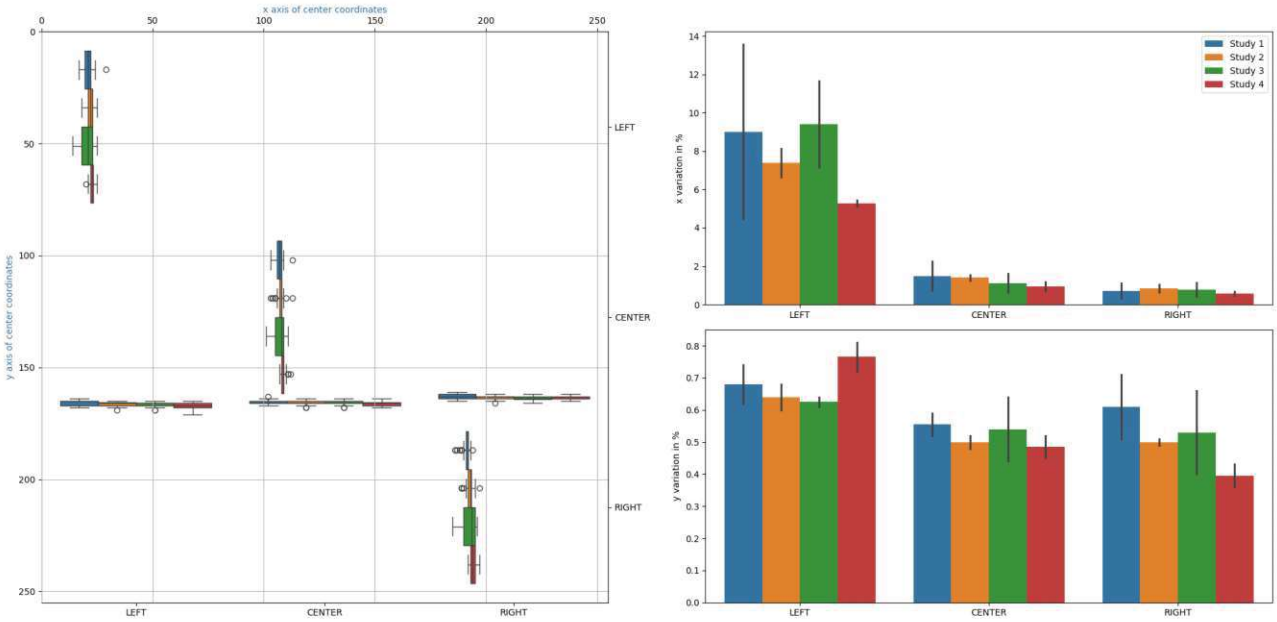


**Figure 30.** Variation in automated ROI positioning for the Zerdine studies

Table 32 and Table 34 shows the percentage error on average for the x- and y-direction in detail within individual studies. Table 33 and Table 35 provide a detailed overview of the average percentage errors across the study sessions 1-4.

| study | position | before | p [%] | p_position [%] | p_study [%] | p_overall [%] |
|---|---|---|---|---|---|---|
| Study_1 | LEFT | before | 13.55 | 9.02 | 3.74 | 3.25 |
| | | after | 4.48 | | | |
| | CENTER | before | 2.24 | 1.49 | | |
| | | after | 0.74 | | | |
| | RIGHT | before | 1.12 | 0.73 | | |
| | | after | 0.33 | | | |
| Study_2 | LEFT | before | 6.65 | 7.39 | 3.21 | |
| | | after | 8.13 | | | |
| | CENTER | before | 1.24 | 1.4 | | |
| | | after | 1.56 | | | |
| | RIGHT | before | 0.63 | 0.84 | | |
| | | after | 1.06 | | | |
| Study_3 | LEFT | before | 11.64 | 9.39 | 3.77 | |
| | | after | 7.15 | | | |
| | CENTER | before | 1.61 | 1.12 | | |
| | | after | 0.63 | | | |
| | RIGHT | before | 1.14 | 0.79 | | |
| | | after | 0.44 | | | |
| Study_4 | LEFT | before | 5.11 | 5.28 | 2.27 | |
| | | after | 5.44 | | | |
| | CENTER | before | 0.7 | 0.93 | | |
| | | after | 1.17 | | | |
| | RIGHT | before | 0.48 | 0.58 | | |
| | | after | 0.69 | | | |

**Table 32.** Percentage error on average for the x-direction in detail; in-study variability

| position | before | p [%] | p_position [%] | p_overall [%] |
|---|---|---|---|---|
| LEFT | True | 12.75 | 9.83 | 4.23 |
| | False | 6.91 | | |
| CENTER | True | 2.17 | 1.75 | |
| | False | 1.34 | | |
| RIGHT | True | 1.31 | 1.09 | |
| | False | 0.88 | | |

**Table 33.** Percentage error on average for the x-direction in detail; variability across study sessions 1-4

| study | position | before | p [%] | p_position [%] | p_study [%] | p_overall [%] |
|---|---|---|---|---|---|---|
| Study_1 | LEFT | before | 0.62 | 0.68 | 0.61 | 0.57 |
| | | after | 0.74 | | | |
| | CENTER | before | 0.52 | 0.55 | | |
| | | after | 0.59 | | | |
| | RIGHT | before | 0.71 | 0.61 | | |
| | | after | 0.51 | | | |
| Study_2 | LEFT | before | 0.68 | 0.64 | 0.55 | |
| | | after | 0.6 | | | |
| | CENTER | before | 0.48 | 0.5 | | |
| | | after | 0.52 | | | |
| | RIGHT | before | 0.49 | 0.5 | | |
| | | after | 0.51 | | | |
| Study_3 | LEFT | before | 0.61 | 0.62 | 0.57 | |
| | | after | 0.64 | | | |
| | CENTER | before | 0.64 | 0.54 | | |
| | | after | 0.44 | | | |
| | RIGHT | before | 0.66 | 0.53 | | |
| | | after | 0.4 | | | |
| Study_4 | LEFT | before | 0.72 | 0.77 | 0.55 | |
| | | after | 0.81 | | | |
| | CENTER | before | 0.45 | 0.48 | | |
| | | after | 0.52 | | | |
| | RIGHT | before | 0.43 | 0.4 | | |
| | | after | 0.36 | | | |

**Table 34.** Percentage error on average for the y-direction in detail; in-study variability

| position | before | p [%] | p_position [%] | p_overall [%] |
|---|---|---|---|---|
| LEFT | True | 0.72 | 0.74 | 0.63 |
| | False | 0.77 | | |
| CENTER | True | 0.54 | 0.55 | |
| | False | 0.55 | | |
| RIGHT | True | 0.64 | 0.59 | |
| | False | 0.54 | | |

**Table 35.** Percentage error on average for the y-direction in detail; variability across study sessions 1-4

The analysis of the x- and y-directions indicated an in-study variation of 3.25% and 0.57%, respectively. Furthermore, an overall variation across study sessions was determined to be 4.23% and 0.63%, respectively. The results indicate that variation in the x-direction is greater than in the y-direction. In the x-direction, the `left` position shows significantly more variation than the `center` and `right` positions, while in the y-direction, the `left` position shows a slightly higher variation compared to the others. This variability was influenced by both the physical repositioning of the detector in its holder and the automated threshold-based evaluation of the center. To assess the relative impact of these factors on overall variation, additional analysis methods would be required, which are beyond the scope of this project.

## 4.10 Prototype Development of the Gel Wax Phantom

One of the primary reasons for seeking an alternative to the Zerdine phantom was the manufacturers' inability to guarantee consistent reproducibility of its optical properties. Additional drawbacks included the high cost of the Zerdine phantom and the potential degradation of its water-based material caused by the loosening of the encapsulation membrane (Figure 31). Nevertheless, the Zerdine phantom served as a model for the gel wax phantom prototype.

**Figure 31.** Dehydrated Zerdine phantom caused by the loosening of the encapsulation membrane

In 3.2.2 Gel Wax Phantom four design objectives for developing the gel wax prototype were outlined. The following sections discusses the extent to which each of these objectives was

successfully implemented.

**a) Uniform acoustic, mechanical and thermoelastic properties, with both the matrix and absorber composed of the same material**
The phantom was composed entirely of the same material. The phantom matrix consisted of sGW with absorbers made from aGW and coated with an sGW shell, which was essential for the molding process.

There still was potential for improvement including following areas: First, it would have been preferable to give the absorbers slight scattering properties. Second, visual inspection revealed air bubbles trapped around the absorber during embedding. Due to the significant impedance difference between air and gel wax, the resulting optoacoustic waves would be highly attenuated at the interface.

Figure 32 compares the method developed during this project with the optimized positioning technique for the absorber introduced by colleagues at iThera following the completion of this work.

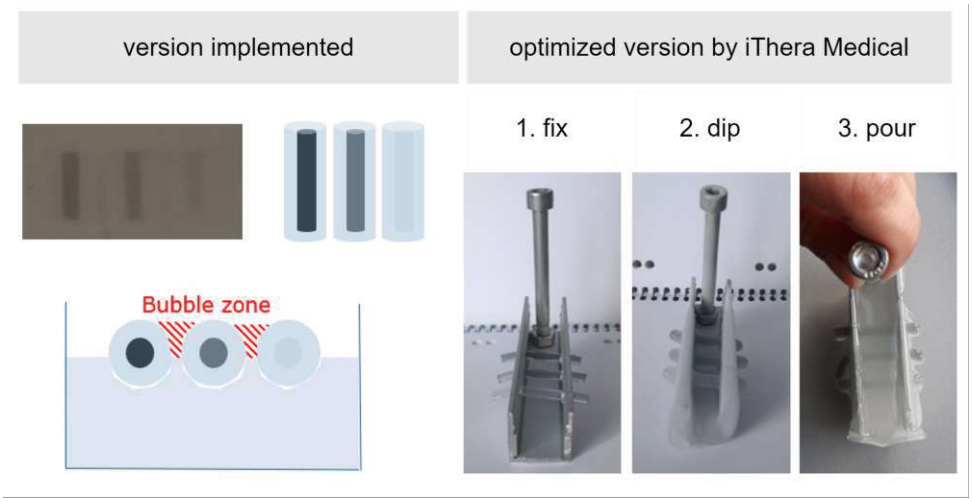


**Figure 32.** Comparison between the implemented method of positioning (left) and the optimized version (right) (image sourced from iThera Medical presentations)

**b) Absorbers of a specified shape, size, position and optical properties representative of biological tissue**
Three embedded absorbers, with known absorption coefficients, dimensions and reproducible positions, were included. The absorption coefficients could be evaluated as described in 3.4 Data Processing and Data Analysis and are shown in Table 36.

| absorber | OD at 800 $nm$ | $\mu_a$ |
|---|---|---|
| 1 | 0.46 | 1.07 |
| 2 | 1.4 | 3.22 |
| 3 | 2.24 | 5.17 |

**Table 36.** Properties of the absorbers in the gel wax phantom prototype

This range of absorption coefficients aligned with measured tissue properties reported in current literature [7, 47–49]. The scattering coefficient ($\mu_s$) of the scattering matrix material could not be assessed due to the unavailability of technology, such as the Double Integrated Sphere employed by Maneas et al. [33]. This limitation presents an opportunity for future research.

**c) Capability to tailor the optical and acoustic properties of the matrix and absorbers**

Similar to other studies [33, 38, 40], the optical properties could be tailored to the requirements by using absorption and scattering materials.

Determining acoustic properties, such as the acoustic absorption coefficient, speed of sound and back-scattering coefficient, required specialized methods and equipment. Exploring whether and how these properties can be individually tailored, or identifying any necessary trade-off, remains an active area of research.

**d) Stable, resistant to bacterial infestation and easy to produce and handle**

Following the recipe described in 3.2.2 Gel Wax Phantom ensures that phantom manufacturing is both straightforward and reproducible. However, the reproducibility of the commercially sourced gel wax batches remained uncertain, as does its impact on the overall consistency of the phantom. No signs of bacterial contamination or dehydration were observed in the gel wax during the project.

The long-term stability of the material's absorbing and scattering properties remains to be assessed, presenting an opportunity for future investigation. According to Jones et al. [40], Ti$O_2$ appears to offer greater stability than monodisperse silica microspheres when used with gel wax.

The gel wax phantom prototype was housed in a 3D-printed protective box, featuring a membrane to guard against contamination. To ensure a reproducible MSOT scans, a sample holder was 3D printed (Figure 33).

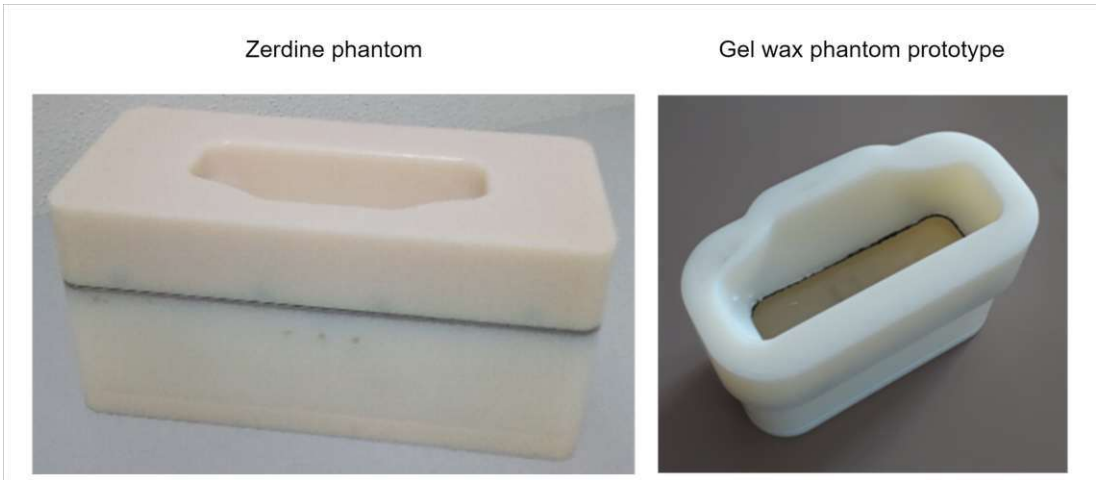


**Figure 33.** Comparison of the Zerdine phantom with the gel wax prototype (image on the right sourced from iThera Medical presentations)

# 5 Conclusion

A calibration phantom tailored for the clinical MSOT Acuity Echo was developed in this study, addressing the need for standardized calibration in light of the device's limitations as of 2018. By using data from an alternative stable phantom, critical aspects of device performance were quantified, including laser stability, noise reduction, signal variability and reproducibility, revealing several challenges that emphasize the necessity of the proposed phantom. These findings not only highlight the potential of the calibration phantom to enhance device reliability but also provide actionable insights into advancing the clinical utility of optoacoustic imaging.

The analysis revealed variability in key performance metrics, including laser stability, signal variability due to absorbers and a dependence of the overall image signal on the imaging target, where higher absorption by the target resulted in uniformly elevated image intensity compared to imaging a low-absorption target at the same location. The proposed calibration phantom is critical not only for accurately characterizing device performance, but also for promoting confidence and precision in optoacoustic imaging as it transitions into clinical use.

While this study successfully demonstrated the need for and potential utility of a calibration phantom in optoacoustic imaging, several opportunities for future work remain. The proposed calibration phantom, primarily designed to emphasize the absorption properties of the material, leaves other physical properties, such as scattering, acoustic, mechanical, and thermoelastic characteristics, open for further evaluation and potential refinement. Investigating alternative materials and configurations might also expand its applicability to a wider range of optoacoustic applications. Moreover, longitudinal studies could evaluate the phantom's ability to maintain calibration accuracy over time and under varying environmental conditions. Beyond device calibration, the phantom's utility could be extended to support research into novel imaging protocols and system optimization, making it a valuable tool for advancing the field of optoacoustic imaging.

# 6 References


[1] Melissa B. Aldrich et al. Seeing it through: translational validation of new medical imaging modalities. *Biomedical Optics Express*, 3(4):764–776, 2012.

[2] Vasilis Ntziachristos. Clinical translation of optical and optoacoustic imaging. *Philosophical Transactions of the Royal Society A: Mathematical, Physical and Engineering Sciences*, 369(1955):4666–4678, 2011.

[3] Yi Qia Balasundarama et al. Navigating challenges and solutions in quantitative photoacoustic imaging. *Applied Physics Reviews*, 10(2):021305, 2023.

[4] Nicolas Goossens et al. Cancer biomarker discovery and validation. *Translational Cancer Research*, 4(3):256–268, 2015.

[5] American College of Radiology. Computed tomography accreditation program: Phantom testing: Ct. https://accreditationsupport.acr.org/support/solutions/articles/11000056197-acr-ct-phantom-scanning-instructions, 2019. Accessed: 2024-11-27.

[6] Lina Hacker, James Joseph, Ledia Lilaj, Srirang Manohar, Aoife M Ivory, Ran Tao, Sarah E Bohndiek, and Members of IPASC. Tutorial on phantoms for photoacoustic imaging applications. *Journal of biomedical optics*, 29(8):080801–080801, 2024.

[7] William C Vogt, Congxian Jia, Keith A Wear, Brian S Garra, and T Joshua Pfefer. Biologically relevant photoacoustic imaging phantoms with tunable optical and acoustic properties. *Journal of biomedical optics*, 21(10):101405–101405, 2016.

[8] Luciana C Cabrelli, Pedro IBGB Pelissari, Alessandro M Deana, Antonio AO Carneiro, and Theo Z Pavan. Stable phantom materials for ultrasound and optical imaging. *Physics in Medicine & Biology*, 62(2):432, 2016.

[9] Martina Fonseca et al. Characterisation of a phantom for multiwavelength quantitative photoacoustic imaging. *Physics in Medicine & Biology*, 61(13):4950–4964, 2016.

[10] iThera Medical. Msot acuity echo - clinical research. https://ithera-medical.com/products/clinical-research/msot-acuity-echo/, 2024. Accessed: 2024-11-11.

[11] Alexander Graham Bell. On selenium and the photophone. *Electrician*, 5:214–220, 1880.

[12] John Tyndall. Iii. action of an intermittent beam of radiant heat upon gaseous matter. *Proceedings of the Royal Society of London*, 31(206-211):307–317, 1881.

[13] Wilhelm C Röntgen. On tones produced by the intermittent irradiation of a gas. *The London, Edinburgh, and Dublin Philosophical Magazine and Journal of Science*, 11(68):308–311, 1881.

[14] LB Kreuzer and CKN Patel. Nitric oxide air pollution: detection by optoacoustic spectroscopy. *Science*, 173(3991):45–47, 1971.

[15] Allan Rosencwaig. Photoacoustic spectroscopy of biological materials. *Science*, 181(4100):657–658, 1973.

[16] Daniel Razansky, Stephan Kellnberger, and Vasilis Ntziachristos. Near-field radiofrequency thermoacoustic tomography with impulse excitation. *Medical physics*, 37(9):4602–4607, 2010.

[17] GJ Diebold, T Sun, and MI Khan. Photoacoustic monopole radiation in one, two, and three dimensions. *Physical review letters*, 67(24):3384, 1991.

[18] GJ Diebold, T Sun, and MI Khan. Photoacoustic waveforms generated by fluid bodies. In *Photoacoustic and Photothermal Phenomena III: Proceedings of the 7th International Topical Meeting, Doorwerth, The Netherlands, August 26–30, 1991*, pages 263–269. Springer, 1992.

[19] T Sun and GJ Diebold. Generation of ultrasonic waves from a layered photoacoustic source. *Nature*, 355(6363):806–808, 1992.

[20] Xosé Luís Deán-Ben and Daniel Razansky. Optoacoustic image formation approaches—a clinical perspective. *Physics in Medicine & Biology*, 64(18):18TR01, 2019.

[21] Hisham Assi, Rui Cao, Madhura Castelino, Ben Cox, Fiona J Gilbert, Janek Gröhl, Kurinchi Gurusamy, Lina Hacker, Aoife M Ivory, James Joseph, et al. A review of a strategic roadmapping exercise to advance clinical translation of photoacoustic imaging: from current barriers to future adoption. *Photoacoustics*, page 100539, 2023.

[22] Konstantin Maslov and Lihong V Wang. Photoacoustic imaging of biological tissue with intensity-modulated continuous-wave laser. *Journal of biomedical optics*, 13(2):024006–024006, 2008.

[23] Srirang Manohar and Daniel Razansky. Photoacoustics: a historical review. *Advances in optics and photonics*, 8(4):586–617, 2016.

[24] Paul Beard. Biomedical photoacoustic imaging. *Interface focus*, 1(4):602–631, 2011.

[25] Huibin Liu, Xiangyu Teng, Shuxuan Yu, Wenguang Yang, Tiantian Kong, and Tangying Liu. Recent advances in photoacoustic imaging: Current status and future perspectives. *Micromachines*, 15(8):1007, 2024.

[26] Sung-Liang Chen, Tao Ling, and L Jay Guo. Low-noise small-size microring ultrasonic detectors for high-resolution photoacoustic imaging. *Journal of Biomedical Optics*, 16(5):056001–056001, 2011.

[27] Rayyan Manwar, Mohsin Zafar, and Qiuyun Xu. Signal and image processing in biomedical photoacoustic imaging: a review. *Optics*, 2(1):1–24, 2020.

[28] Seongyi Han, Dakyeon Lee, Sungjee Kim, Hyung-Hoi Kim, Sanghwa Jeong, and Jeesu Kim. Contrast agents for photoacoustic imaging: a review focusing on the wavelength range. *Biosensors*, 12(8):594, 2022.

[29] Mason W Schellenberg and Heather K Hunt. Hand-held optoacoustic imaging: A review. *Photoacoustics*, 11:14–27, 2018.

[30] Jun Xia, Junjie Yao, and Lihong V Wang. Photoacoustic tomography: principles and advances. *Electromagnetic waves (Cambridge, Mass.)*, 147:1, 2014.

[31] Martha Z Vardaki and Nikolaos Kourkoumelis. Tissue phantoms for biomedical applications in raman spectroscopy: a review. *Biomedical engineering and computational biology*, 11:1179597220948100, 2020.

[32] Sarah E Bohndiek, Sandhya Bodapati, Dominique Van De Sompel, Sri-Rajasekhar Kothapalli, and Sanjiv S Gambhir. Development and application of stable phantoms for the evaluation of photoacoustic imaging instruments. *PloS one*, 8(9):e75533, 2013.

[33] Efthymios Maneas, Wenfeng Xia, Olumide Ogunlade, Martina Fonseca, Daniil I Nikitichev, Anna L David, Simeon J West, Sebastien Ourselin, Jeremy C Hebden, Tom Vercauteren, et al. Gel wax-based tissue-mimicking phantoms for multispectral photoacoustic imaging. *Biomedical optics express*, 9(3):1151–1163, 2018.

[34] Gloria M Spirou, Alexander A Oraevsky, I Alex Vitkin, and William M Whelan. Optical and acoustic properties at 1064 nm of polyvinyl chloride-plastisol for use as a tissue phantom in biomedical optoacoustics. *Physics in Medicine & Biology*, 50(14):N141, 2005.

[35] Sílvio L Vieira, Theo Z Pavan, Jorge E Junior, and Antonio AO Carneiro. Paraffin-gel tissue-mimicking material for ultrasound-guided needle biopsy phantom. *Ultrasound in medicine & biology*, 39(12):2477–2484, 2013.

[36] Efthymios Maneas, Wenfeng Xia, Daniil I Nikitichev, Batol Daher, Maniragav Manimaran, Rui Yen J Wong, Chia-Wei Chang, Benyamin Rahmani, Claudio Capelli, Silvia Schievano, et al. Anatomically realistic ultrasound phantoms using gel wax with 3d printed moulds. *Physics in Medicine & Biology*, 63(1):015033, 2018.

[37] Ronald X Xu, Joseph Ewing, Hamid El-Dahdah, Bei Wang, and Stephen P Povoski. Design and benchtop validation of a handheld integrated dynamic breast imaging system for noninvasive characterization of suspicious breast lesions. *Technology in cancer research & treatment*, 7(6):471–481, 2008.

[38] Erbao Dong, Zuhua Zhao, Minjie Wang, Yanjun Xie, Shidi Li, Pengfei Shao, Liuquan Cheng, and Ronald X Xu. Three-dimensional fuse deposition modeling of tissue-simulating phantom for biomedical optical imaging. *Journal of Biomedical Optics*, 20(12):121311–121311, 2015.

[39] Aoife M Ivory, Anant Shah, Srinath Rajagopal, and Bajram Zeqiri. Development and investigation of the acoustic properties of tissue-mimicking materials for photoacoustic imaging techniques. In *2019 IEEE International Ultrasonics Symposium (IUS)*, pages 1489–1492. IEEE, 2019.

[40] Charlotte J Maughan Jones and Peter RT Munro. Stability of gel wax based optical scattering phantoms. *Biomedical Optics Express*, 9(8):3495–3502, 2018.

[41] IPASC. Ipasc. https://www.ipasc.science/ipasc.science/, 2024. Accessed: 2024-11-27.

[42] Christian Richter, Gloria Spirou, Alexander A Oraevsky, William M Whelan, and Michael C Kolios. Examination of contrast mechanisms in optoacoustic imaging of thermal lesions. In *Photons Plus Ultrasound: Imaging and Sensing 2006: The Seventh Conference on Biomedical Thermoacoustics, Optoacoustics, and Acousto-optics*, volume 6086, pages 406–415. SPIE, 2006.

[43] Robert A Kruger, Richard B Lam, Daniel R Reinecke, Stephen P Del Rio, and Ryan P Doyle. Photoacoustic angiography of the breast. *Medical physics*, 37(11):6096–6100, 2010.

[44] Brian W Pogue and Michael S Patterson. Review of tissue simulating phantoms for optical spectroscopy, imaging and dosimetry. *Journal of biomedical optics*, 11(4):041102–041102, 2006.

[45] Martin O Culjat, David Goldenberg, Priyamvada Tewari, and Rahul S Singh. A review of tissue substitutes for ultrasound imaging. *Ultrasound in medicine & biology*, 36(6):861–873, 2010.

[46] Vasilis Ntziachristos. Going deeper than microscopy: the optical imaging frontier in biology. *Nature methods*, 7(8):603–614, 2010.

[47] Oleksii Sieryi, Alexey Popov, Vyacheslav Kalchenko, Alexander Bykov, and Igor Meglinski. Tissue-mimicking phantoms for biomedical applications. In *Tissue Optics and Photonics*, volume 11363, pages 111–117. SPIE, 2020.

[48] Pan Li, Zhiyong Yang, and Shan Jiang. Tissue mimicking materials in image-guided needle-based interventions: A review. *Materials Science and Engineering: C*, 93:1116–1131, 2018.

[49] Wai-Fung Cheong, Scott A Prahl, and Ashley J Welch. A review of the optical properties of biological tissues. *IEEE journal of quantum electronics*, 26(12):2166–2185, 1990.

# 7 List of Acronyms and Abbreviations

| | |
|---|---|
| **MSOT** | Multispectral optoacoustic tomography |
| **IPACS** | International Photoacoustic Standardization Consortium |
| **CIRS** | CIRS is now Sun Nuclear |
| **FOV** | Field of view |
| **ROI** | Region of interest |
| **3D** | Three-dimensional |
| **2D** | Two-dimensional |
| **PE** | Polyethylene |
| **PVA** | Polyvinyl alcohol |
| **SEBS** | Styrene-ethylene/butylene-styrene |
| **PVCP** | Polyvinyl chloride plastisol |
| **PMMA** | Poly-methyl methacrylate |
| **VAT** | Virtual Area of Transfer |
| **Ti**$O_2$ | Titandioxid |
| **cGW** | Clear gel wax |
| **sGW** | Scattering gel wax |
| **aGW** | Absorbing gel wax |
| **asGW** | Absorbing-scattering gel wax |
| **hcsGWp** | High-concentration scattering gel wax pallet |
| **hcasGWp** | High-concentration absorbing-scattering gel wax pallet |
| **aGWia** | Absorbing gel wax inclusion amounts |
| **asGWia** | Absorbing-scattering gel wax inclusion amounts |
| **FFT** | Fast Fourier Transformation |
| **OD** | Optical density |
| **A** | Absorbance |

**Table 37.** List of acronyms and abbreviations

# 8 List of Figures

# 9 List of Tables

# 10 Acknowledgements

I would like to extend my heartfelt thanks to everyone who supported me in completing this work.

A special thanks goes to Stefan Morscher from iThera Medical GmbH. His expertise, guidance and encouragement were invaluable to me. His insights and support during my time at iThera Medical GmbH had a significant impact on both this research and my professional development.

I am also deeply grateful to Ao.Univ.-Prof.i.R. Dipl.-Ing. Dr.techn. Martin Gröschl for his academic guidance and valuable feedback. The collaboration between iThera Medical GmbH and TU Wien was a truly enriching experience for me.

My sincere appreciation goes to my colleagues at iThera Medical GmbH for their great teamwork, meaningful discussions and overall support throughout this project. Their professionalism and camaraderie made this period both rewarding and enjoyable. A special mention to Ruben Moreno for his dedicated assistance with the development and production of the phantom.

I would also like to thank the International Office for their generous financial support during my research.

Finally, I am immensely grateful to my family and friends for their unwavering encouragement and belief in me. Their support was a tremendous help during this challenging yet fulfilling journey.